

# Computational Infrared and Two-Dimensional Infrared Photon Echo Spectroscopy of Both Wild-Type and Double Mutant Myoglobin-CO Proteins

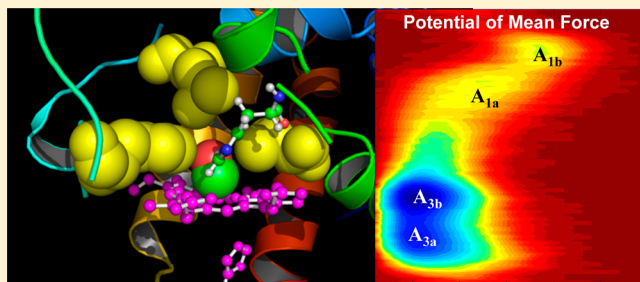
Jun-Ho Choi,<sup>†</sup> Kyung-Won Kwak,<sup>\*,‡</sup> and Minhaeng Cho<sup>\*,†</sup>

<sup>†</sup>Department of Chemistry, Korea University, Seoul 136-713, Korea

<sup>‡</sup>Department of Chemistry, Chung-Ang University, Seoul 156-756, Korea

 Supporting Information

**ABSTRACT:** The CO stretching mode of both wild-type and double mutant (T67R/S92D) MbCO (carbonmonoxymyoglobin) proteins is an ideal infrared (IR) probe for studying the local electrostatic environment inside the myoglobin heme pocket. Recently, to elucidate the conformational switching dynamics between two distinguishable states, extensive IR absorption, IR pump–probe, and two-dimensional (2D) IR spectroscopic studies for various mutant MbCO's have been performed by the Fayer group. They showed that the 2D IR spectroscopy of the double mutant, which has a peroxidase enzyme activity, reveals a rapid chemical exchange between two distinct states, whereas that of the wild-type does not. Despite the fact that a few simulation studies on these systems were already performed and reported, such complicated experimental results have not been fully reproduced nor described in terms of conformational state-to-state transition processes. Here, we first develop a distributed vibrational solvatochromic charge model for describing the CO stretch frequency shift reflecting local electric potential changes. Then, by carrying out molecular dynamic simulations of the two MbCO's and examining their CO frequency trajectories, it becomes possible to identify a proper reaction coordinate consisting of His64 imidazole ring rotation and its distance to the CO ligand. From the 2D surfaces of the resulting potential of mean forces, the spectroscopically distinguished  $A_1$  and  $A_3$  states of the wild-type as well as two more substates of the double mutant are identified and their vibrational frequencies and distributions are separately examined. Our simulated IR absorption and 2D IR spectra of the two MbCO's are directly compared with the previous experimental results reported by the Fayer group. The chemical exchange rate constants extracted from the two-state kinetic analyses of the simulated 2D IR spectra are in excellent agreement with the experimental values. On the basis of the quantitative agreement between the simulated spectra and experimental ones, we further examine the conformational differences in the heme pockets of the two proteins and show that the double mutation, T67R/S92D, suppresses the  $A_1$  population, restricts the imidazole ring rotation, and increases hydrogen-bond strength between the imidazole  $N_e$ –H and the oxygen atom of the CO ligand. It is believed that such delicate change of distal His64 imidazole ring dynamics induced by the double mutation may be responsible for its enhanced peroxidase catalytic activity as compared to the wild-type myoglobin.



## I. INTRODUCTION

Mutation is one of the most direct procedures to introduce local structural changes in proteins, which often result in the modulation of their biological functions as well as the alteration of secondary and tertiary structural stabilities. From a simple mechanical viewpoint, it is quite interesting that complex protein functions are sometimes strongly affected by just one or two substitutions of residues with natural or unnatural amino acids.<sup>1–5</sup> Nonetheless, the folded structure of protein naturally optimizes the global free energy via reconfiguring the involved interactions among various components in proteins.<sup>6–9</sup> Often, such mutations induce variations in steric hindrance and charge distribution, which then propagate into neighboring sites through molecular interactions and affect local or global structure and even protein functions.<sup>4,10</sup> Due to the local

nature of such site mutation, experimental methods with a local probe are desired to investigate its subsequent effects. Among them, a variety of vibrational spectroscopic methods focusing on specially designed molecular oscillators, known as infrared (IR) probes,<sup>11</sup> have been extensively used to measure local electric field changes induced by mutations.<sup>12–24</sup> Over the years, a variety of IR probes that can be readily incorporated into proteins and DNAs in a site-specific manner have been effectively used to investigate the biomolecular structure and dynamics.<sup>11,16,19,25–34</sup>

**Special Issue:** Michael D. Fayer Festschrift

**Received:** May 27, 2013

**Revised:** July 16, 2013

**Published:** July 19, 2013



One of the most accurately measurable quantities in vibrational spectroscopy is the frequency shift of a given IR probe as compared to its frequency measured for proteins before site-specific mutations. Thus, the vibrational frequency shift measurements are considered to be an efficient way to infer possible local structural changes and consequent electric field modulations around an IR probe. Although IR absorption spectroscopy is enough to accurately measure the resonant frequency, the vibrational Stark effect spectroscopy can be considered as a complementary tool for measuring local electric field if the vibrational solvatochromic dipole contribution to the frequency shift is the dominant term.<sup>35–40</sup> However, it is the time-resolved nonlinear IR spectroscopy that is capable of providing critical information on the magnitude and time scale of solute–solvent interaction-induced frequency fluctuations.<sup>41,42</sup> In fact, various spectroscopic studies of the protein's structural dynamics are based on one of the most critical assumptions that there is a direct one-to-one correspondence between the vibrational state and the corresponding structure. That is to say, one vibrational state represents one structure. However, there are cases that such precise assignment of the structural origin of the vibrational state is uncertain.<sup>43–45</sup> Then, the molecular dynamics (MD) simulations using properly developed theoretical models are absolutely necessary to remove potential ambiguities in spectroscopic assignments.<sup>18,46</sup>

The IR absorption, IR pump–probe, and two-dimensional (2D) IR photon echo spectroscopy have been extensively used to extract valuable dynamic information on protein conformational change and chemical exchange between two shortly surviving species or states in real time.<sup>41,42,47–52</sup> Among various proteins studied, myoglobin (Mb) with a small ligand such as CO, NO, O<sub>2</sub>, CN<sup>−</sup>, or N<sub>3</sub><sup>−</sup> has been one of the main targets for time-resolved spectroscopic investigation because it is an ideal prototype model system for understanding the enzyme–ligand binding and dissociation processes in time.<sup>6,53–75</sup> Furthermore, it has been shown that certain Mb mutant proteins exhibit a catalytic activity.<sup>5,10</sup> Recently, the Fayer group carried out 2D IR photon echo studies of two mutants, L29I and T67R/S92D, and measured the time constants associated with conformational transition between the so-called A<sub>1</sub> and A<sub>3</sub> states.<sup>18,61</sup> Here, the stretching mode of CO binding to Mb heme, denoted as MbCO, was used as an IR probe reporting local structural change around CO. The corresponding IR absorption spectrum appears to be highly asymmetric, and there is a low-frequency shoulder peak. These two spectroscopically distinguishable peaks were assigned to the A<sub>1</sub> ( $\sim$ 1944 cm<sup>−1</sup>) and A<sub>3</sub> ( $\sim$ 1932 cm<sup>−1</sup>) states. Bagchi et al. observed the chemical exchange between these two states of the double mutant Mb (T67R/S92D), carrying out numerical analysis on the time-dependent diagonal and cross peak volumes extracted from a series of time-resolved 2D IR spectra.<sup>18</sup> Here, double mutant Mb was produced by introducing a distal arginine and a proximal aspartate to the wild-type Mb. It was shown that such site-directed double mutation of Mb induces a significant enhancement of the peroxidase catalytic activity as compared to the wild-type.<sup>10</sup> Similar to the FTIR spectrum of the wild-type MbCO, that of the double mutant also exhibits two peaks, though their relative intensities are significantly different from those of the wild-type. Nonetheless, the two peaks were regarded as the same A<sub>1</sub> and A<sub>3</sub> states, because their frequencies remain the same regardless of double mutation.<sup>18</sup> A critical difference in the two spectra of wild-type and double mutant is that, for the double mutant (wild-type), the A<sub>3</sub> (A<sub>1</sub>) band

intensity appears to be stronger than the A<sub>1</sub> (A<sub>3</sub>). Recent molecular dynamic (MD) simulation studies showed that the distal histidine, His64, plays an important role in determining the CO stretch frequency in these cases.<sup>18,46</sup> However, due to a lack of quantitative model for predicting CO stretch frequency shift and fluctuation induced by its local interaction with surrounding amino acid residues, the experimentally measured IR absorption and 2D IR spectra have not been fully reproduced theoretically.<sup>18,43,46</sup>

Although the 2D IR experiments revealed various dynamics in proteins occurring on a fast time scale, they do not give a direct and detailed microscopic picture on the mutation effect itself. In this regard, statistical analyses of the QM/MM (quantum mechanical/molecular mechanical) MD trajectories could provide invaluable information about the local environment around an enzyme active site.<sup>43,76</sup> However, the MD trajectories themselves cannot be easily translated into spectroscopic observables that can be directly compared with experiment results. Therefore, it is absolutely prerequisite for successful interpretation of highly complicated spectroscopic data such as 2D IR spectra to develop proper theoretical models that connect structural data extracted from MD trajectories with spectroscopic signals of the system. This begins with developing vibrational solvatochromism models that are useful to calculate the solvatochromic frequency shifts of various IR probes in condensed phases including solutions and proteins.<sup>77–79</sup> Among them, the vibrational Stark effect theory for vibrational solvatochromic frequency shift prediction has been widely used,<sup>37,39,80</sup> where the vibrational frequency shift is assumed to be given as  $\Delta\omega = -\Delta\mu_{\text{Stark}} \cdot \Delta E$ . Here,  $\Delta\omega$  is the frequency shift induced by a small change of local electric field  $\Delta E$  and  $\Delta\mu_{\text{Stark}}$  is known as the vibrational Stark tuning rate. Once  $|\Delta\mu_{\text{Stark}}|$  is independently measured for a given IR probe, the frequency shift measurement can be used to estimate the local electric field change, by using the above linear relationship between  $\Delta\omega$  and  $\Delta E$ . There already exist quite interesting theoretical studies and attempts to numerically simulate the IR absorption spectra of wild-type and mutant MbCO's with employing this vibrational Stark theory in combination with MD simulations of the wild-type and the double mutant.<sup>18,46</sup> In particular, Merchant et al. were able to identify two distinguished conformational states denoted as A<sub>1</sub> and A<sub>3</sub>, examining their simulated IR absorption spectrum of the wild-type.<sup>46</sup> They further showed that dynamic motion of His64 is responsible for vibrational dephasing of the A<sub>3</sub> band in the low-frequency region. For the double mutant, Bagchi et al. studied the two frequency-resolved IR peaks by calculating frequency–frequency correlation functions with MD trajectories.<sup>18</sup> However, it was unfortunate that their simulation results were not consistent with the experimentally measured interconversion rates between A<sub>1</sub> and A<sub>3</sub> states by the Fayer group.

Despite the fact that these MD simulation studies have provided detailed information on local structures around CO ligand in the wild-type and double mutant, there are a few important issues that have not been fully understood yet. First of all, it is necessary to understand how detailed structural differences in the two (wild-type and double mutant) MbCO systems affect their IR spectra. To achieve this goal, one should have a quantitatively reliable model for predicting vibrational frequency shifts of CO stretching mode in MbCO upon local structural changes. We here develop a new model beyond the vibrational Stark effect theory. Only then does the spectro-

scopic assignment of each peak in the IR spectra become possible. The second important issue is to develop a computational method for simulating the 2D IR spectra of these MbCO's, which can then be directly compared with previously reported experimental spectra. Once the numerically simulated 2D IR spectra are in quantitative agreement with the experimental results, we will be able to explain why the cross peaks are clearly visible in the 2D IR spectra of double mutant MbCO but they are not for wild-type MbCO.

In this work, we first develop a distributed vibrational solvatochromic charge model to calculate the CO stretch frequency of MbCO.<sup>77,78</sup> Then, carrying out extensive MD simulations, we obtain fluctuating frequency shift trajectories, which are then used to simulate both IR absorption and 2D IR spectra for direct comparisons with experimental results. The agreement between the simulation and the experimental results are quantitative, as will be shown in this paper. Furthermore, the chemical exchange rates estimated by using the present computational studies are found to be in good agreement with those obtained by the Fayer group.<sup>18,46</sup> This indicates that the vibrational solvatochromism model developed here is reliable and the MD trajectories faithfully mimic the real dynamics of the heme pocket in these MbCO's. Carefully examining the calculated potential of mean forces (PMF) with properly chosen reaction coordinates for interconversions between multiple substates, we show that the previous spectroscopic assignments of peaks in the vibrational spectra need to be slightly modified and generalized. Finally, the structural difference between the wild-type and the double mutant MbCO's and its influence on the enhanced peroxidase catalytic activity of the double mutant are discussed.

## II. QUANTUM CHEMISTRY CALCULATIONS AND VIBRATIONAL SOLVATOCHROMISM

In this section, we present a detailed description about solvatochromic frequency shift calculation method with considering a set of distributed interaction sites. The heme–CO complex in the active site of MbCO interacts with surrounding residues and water molecules. The solvent electric field due to polar side-chains of neighboring residues is spatially nonuniform so that the validity of the vibrational Stark effect theory for this heterogeneous environment should be examined. In fact, our recent studies for a variety of small IR probes such as NC-, NCS-, NCSe, and N<sub>3</sub>-derivatized molecules and amino-acids revealed that the vibrational solvatochromic dipole ( $\Delta\mu$ ) is not the dominant factor in determining their frequency shifts induced by solute–solvent electrostatic interactions.<sup>81</sup> Therefore, here a theoretical model beyond the dipole–dipole approximation to intermolecular interaction is needed.

It was shown that the vibrational frequency shift can be approximately written as<sup>77</sup>

$$\Delta\omega = \omega - \omega_0 = \sum_{x=1}^N l_x \phi(\mathbf{R}_x) \quad (1)$$

where the linear expansion coefficient  $l_x$  represents the vibrational solvatochromic charge of the  $x$ th site interacting with local solvent electric potential  $\phi(\mathbf{R}_x)$ . Here, the number of interaction sites is  $N$ . In eq 1, the vibrational frequency of an isolated IR probe, which is the heme–CO complex itself, is denoted as  $\omega_0$ . To determine the vibrational solvatochromic charges  $\{l_x\}$ , we used quantum chemistry calculation results

that include coordinates of surrounding “solvent” molecules around CO. Since the partial charges of amino acid residues and water molecules are known, one can directly calculate the electric potential  $\phi(\mathbf{R})$  around CO. Furthermore, the quantum chemistry vibrational analyses of the clusters containing heme–CO and “solvent” molecules provide harmonic frequency  $\omega$  for each cluster. Thus, the array of data consisting of  $\Delta\omega$  and  $\{\phi(\mathbf{R}_x)\}$  values can be used to obtain  $\{l_x\}$  by carrying out a multivariate least-squares fitting analysis with eq 1.

**A. Determination of  $l$ -Parameters within a Variety of Heme–CO Clusters.** Here, we consider a variety of clusters, where the heme–CO complex is surrounded by water molecules, neutral histidine (with N<sub>ε</sub>–H) representing distal His64, neutral histidine with N<sub>δ</sub>–H representing proximal His93, and also positively charged histidine and arginine residues (see Figure 1), which are also found inside the heme

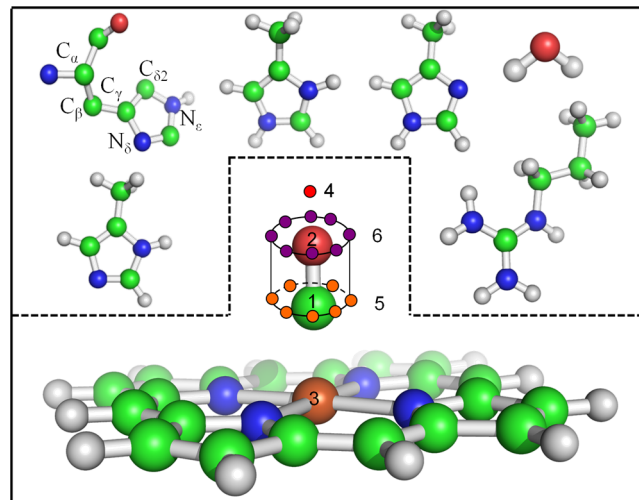


**Figure 1.** Distributed vibrational solvatochromic charge model for predicting the frequency shift of CO stretch mode in the heme–CO complex model. Here, for quantum chemistry calculations, we considered various complexes containing a heme–CO and model compounds (see figure for chemical structures) that approximately represent the polar side chains of residues found in the myoglobin heme pocket. In addition to the neutral histidine (His) model that is methylated imidazole, positively charged methylated imidazole that is protonated at the N<sub>ε</sub> or N<sub>δ</sub> atom is also considered as a model compound for positively charged histidines. The compound on the right is a model for positively charged arginine (Arg).

pocket. The IR probe is the heme–CO complex instead of an isolated CO, where the CO ligand forms a very strong  $d-\pi^*$  back bonding interaction with an Fe atom. Such interaction makes the CO dipole strength large and the CO frequency red-shift as compared to those of an isolated CO.<sup>38,80</sup>

We first performed geometry optimizations for all the clusters with restraining the distances between the O-atom of CO and surrounding residue molecules using Gaussian 09 program with B3LYP/6-31G(d) basis set.<sup>82</sup> With the same basis set, the harmonic frequency of the CO stretch mode was calculated for each cluster. As shown in Figure 1, we considered 20 distributed sites. The first three sites are located at the C, O, and Fe atoms. The additional site 4 is on the CO axis and away from O atom by 0.7 Å, which represents the lone pair electron orbital. The eight circularly distributed sites around the C and O atoms are on the rim of the circle with radius of 0.7 Å, and they represent electronic distributions of CO  $\pi$  orbitals. Those

*l*-parameters of eight circularly distributed sites are assumed to be the same. Ignoring charge transfer between heme–CO and neighboring residues, we have  $\sum_{x=1}^N l_x = 0$ . Consequently, the total number of independent *l*-parameters (in *e*) is 5. We took into consideration 60 different cluster configurations for quantum chemistry calculations. The “solvent” electric potential was calculated by using the Mulliken atomic partial charges of surrounding molecules (see Figure 1). Then, using eq 1 and carrying out multivariate least-squares fitting analyses for those quantum chemistry calculation results, we obtained all the vibrational solvatochromic charges:  $l_1 = 0.074066$ ,  $l_2 = 0.033654$ ,  $l_3 = -0.0052982$ ,  $l_4 = -0.0015472$ ,  $l_5 = -0.0063286$ , and  $l_6 = -0.0062807$ . Here, the reference frequency of the heme-bound CO stretch mode is 2089.7  $\text{cm}^{-1}$ —note that the B3LYP/6-31G-calculated CO frequency in the gas phase is 2208.6  $\text{cm}^{-1}$ . To examine the fitting quality, the DFT (density functional theory) calculated frequency shifts are directly compared with the fitting results (see Figure 2).

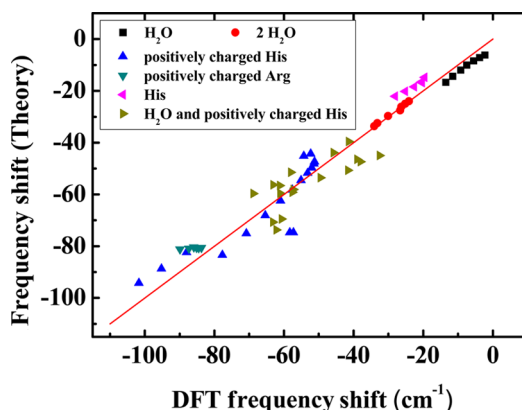


**Figure 2.** DFT-calculated vibrational frequency shift vs theoretically calculated frequency shift with eq 1. Here, 60 different configurations of heme–CO + surrounding model compounds (shown in Figure 1) were considered.

The correlation coefficient is 0.95, which suggests that the distributed interaction sites, collectively acting like an antenna system for sensing local electric potential were properly selected.

**B. Multipole Expansion Approximation.** Instead of the distributed vibrational solvatochromic charge model in eq 1, vibrational solvatochromic multipole model could also be of use and allows us to test the validity of vibrational Stark effect theory—note that, if the vibrational solvatochromic dipole term is dominant over the other higher multipole terms, the vibrational Stark effect theory might be a good approximate model for describing vibrational solvatochromic frequency shift.<sup>77,81</sup> Much like the multipole expansion of distributed charges to approximately describe intermolecular Coulomb interaction, one can take the multipole expansion of distributed vibrational solvatochromic charges so that the frequency shift can be approximately given as<sup>81</sup>

$$\Delta\omega(\phi) = -\Delta\mu \cdot \mathbf{E}(0) - \frac{1}{6}\Delta\Theta \otimes \nabla\mathbf{E}(0) \\ - \frac{1}{30}\Delta\Omega \otimes \nabla\nabla\mathbf{E}(0) \dots \quad (2)$$

where the vector or tensor elements of the vibrational solvatochromic dipole, quadrupole, and octupole are, respectively,

$$[\Delta\mu]_i = \sum_{x=1} l_x [\mathbf{R}_x]_i$$

$$[\Delta\Theta]_{ij} = \sum_{x=1} l_x \{3[\mathbf{R}_x]_i [\mathbf{R}_x]_j - |\mathbf{R}_x|^2 \delta_{ij}\}$$

$$[\Delta\Omega]_{ijk} \equiv \sum_{x=1} l_x \{5[\mathbf{R}_x]_i [\mathbf{R}_x]_j [\mathbf{R}_x]_k - |\mathbf{R}_x|^2 \}$$

$$\{([\mathbf{R}_x]_i \delta_{jk} + [\mathbf{R}_x]_j \delta_{ik} + [\mathbf{R}_x]_k \delta_{ij})\}$$

Recently, we showed that the vibrational solvatochromic quadrupole or even octupole contributions to the frequency shift are not negligibly small in the cases of the IR probes containing nitrile, thiocyanato, and azido groups.<sup>81</sup> Particularly, to calculate the frequency shifts of CO surrounded by water molecules, we found that both the dipole and quadrupole contributions should be equally taken into account. It was also shown that the center of square eigenvector element (COE) is an appropriate choice for the origin of vibrational solvatochromic multipoles,<sup>81</sup> where the position of COE is defined as

$$\mathbf{R}_{\text{COE}} = \sum_j \{L_{j,x}^2 [\mathbf{r}_j]_x \hat{x} + L_{j,y}^2 [\mathbf{r}_j]_y \hat{y} + L_{j,z}^2 [\mathbf{r}_j]_z \hat{z}\} \quad (3)$$

Here, the *x*-component of the mass-weighted eigenvector element of the *j*th atom is denoted as  $L_{j,x}$  for a given normal mode. The dipole and quadrupole contributions to the frequency shift, which correspond to the first and second terms in eq 2, are separately plotted in Figure 3. It turns out

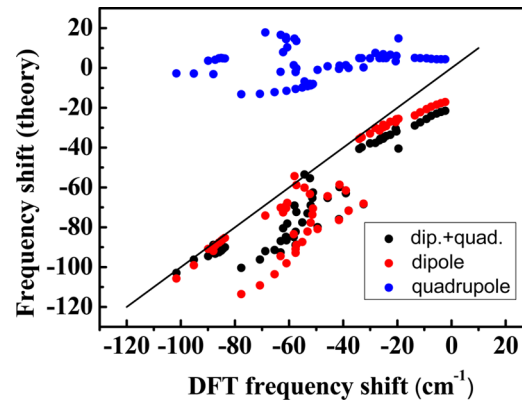


**Figure 3.** DFT-calculated vibrational frequency shift vs theoretically calculated frequency shift. Here, the vibrational solvatochromic dipolar and quadrupolar contributions to the frequency shifts are separately plotted (red and blue closed circles, respectively). The black circles result from dipole + quadrupole terms.

that the vibrational solvatochromic dipole is the dominant factor for the solvatochromic frequency shift in this case, which indicates that the vibrational Stark effect theory is not an unacceptable approach in this particular case of the heme–CO system in myoglobin. However, it should be noted that the multipolar expansion theory in eq 2 (see the black circles in Figure 3) typically overestimate the frequency shift. Consequently, we believe that the distributed vibrational solvatochromic charge model in eq 1 works better than the Stark effect theory even in this case (compare Figures 2 and 3).

To further show that our vibrational solvatochromic charges are quantitatively reliable, we calculate the vibrational Stark tuning rate and compare it with the experimentally measured value reported by Boxer and co-workers.<sup>38,80</sup> We showed that

the vibrational Stark tuning vector  $\Delta\mu_{\text{Stark}}$  is directly related to the vibrational solvatochromic charges as

$$\Delta\mu_{\text{Stark}} = \hbar \sum_{j=1}^N l_j \mathbf{R}_j \quad (4)$$

where  $\mathbf{R}_j$  is the position vector of the  $j$ th site. A proper conversion factor to obtain  $\Delta\mu/\hbar$  value in inverse centimeters per megavolt per centimeter was given in ref 77. From our  $\{l_x\}$  with eq 4, we found that  $|\Delta\mu/\hbar|$  of CO stretch mode of heme-CO complex is  $0.82 \text{ cm}^{-1}(\text{MV}/\text{cm})^{-1}$ —note that the experimental value of  $|\Delta\mu/f/\hbar|$  is  $1.8\text{--}2.2 \text{ cm}^{-1}(\text{MV}/\text{cm})^{-1}$ , where  $f$  is the local field correction factor in the range from 1.1 to 1.3.<sup>38,83</sup> Although our value is smaller than the experimental result, it should be noted that the absolute magnitudes of solvatochromic charges and thereby vibrational Stark tuning rate are strongly dependent on partial charges of surrounding molecules like water, His, and Arg in the heme pocket. In the present work, we used the AMBER partial charges. In fact, a similar value of  $1.0 \text{ cm}^{-1}(\text{MV}/\text{cm})^{-1}$  was used by Bagchi et al. to quantitatively reproduce the IR absorption spectrum of the double mutant (T67R/S92D) MbCO,<sup>18</sup> where they also used the AMBER force field. The present computational result of  $|\Delta\mu/\hbar| = 0.82 \text{ cm}^{-1}(\text{MV}/\text{cm})^{-1}$  supports the adjusted value of  $|\Delta\mu/\hbar|$  in ref 18 to some extent. Furthermore, the fact that our theoretically predicted value of  $|\Delta\mu/\hbar|$  is smaller than the experimental value obtained by the Boxer group suggests that the atomic partial charges implemented in the AMBER program<sup>84</sup> may well be a bit overestimated. Nevertheless, in the present work, the distributed vibrational solvatochromic charge model in eq 1 is used for the sake of improved computational accuracy.

### III. MD SIMULATION AND REACTION COORDINATE

**A. MD Simulation Method.** For MD simulations of MbCO, the X-ray structure of the wild-type MbCO (PDB code = 1MBC) containing 153 residues and a heme moiety was used.<sup>85</sup> The structure of the double mutant was constructed by using the PDB file (1HIX) and replacing the CN<sup>-</sup> ligand with CO (see Figure 4).<sup>10</sup> The AMBER 9 simulation package was used.<sup>84</sup> The partial charges of C and O atoms are assumed to be 0.174 and  $-0.174 \text{ e}$ , respectively, which were newly determined by performing quantum chemistry calculation with the B3LYP/6-31G(d) method. These are in fact similar to those (0.17 and  $-0.17 \text{ e}$ , respectively) used before for MD simulations of carboxy neuroglobin.<sup>86</sup> The water molecules in the X-ray structure were removed and 6999 and 7119 water molecules were added to the simulation box containing a single wild-type or double mutant MbCO, respectively. One chloride ion was added to the simulation box of double mutant MbCO for charge neutralization of the whole system. The TIP3P force-field water was used and periodic boundary condition was imposed. Long-range electrostatic interactions were treated by the particle-mesh Ewald method implemented in the AMBER program.<sup>87</sup> Before carrying out MD simulations, the entire composite system was energy-minimized with the steepest descent method and the conjugate gradient method. Subsequently, it was equilibrated at constant pressure of 1 atm and temperature of 298 K with a 1 fs time step for 500 ps to adjust the periodic box size. Finally, after an additional constant temperature simulation at 298 K for another 500 ps, the production run was performed for 10 ns to obtain an ensemble

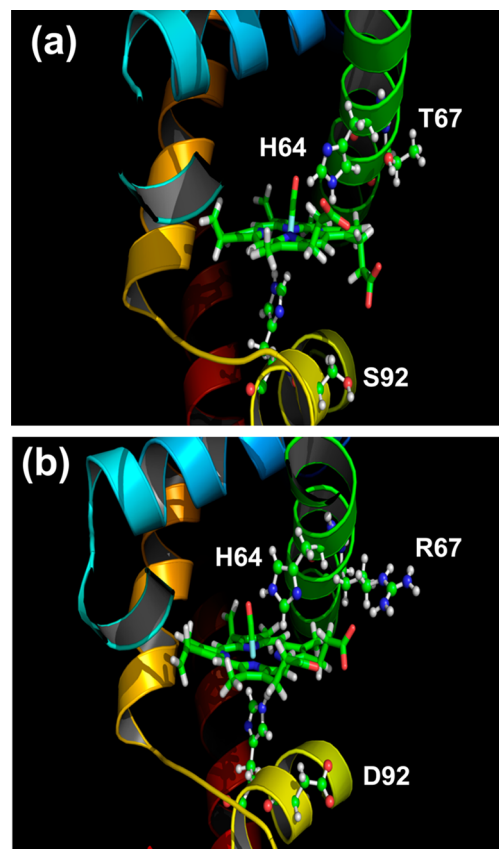


**Figure 4.** Ensemble-averaged structures of wild-type and double mutant MbCO's obtained from the (500 ps, NVT) MD trajectories. The two residues, Thr67(T67) and Ser92(S92), in the wild-type MbCO are replaced with Arg67(R67) and Asp92(D92) residues in the double mutant.

of protein structures, where trajectories were saved for every 50 fs to calculate various time-correlation functions.

**B. CO Stretch Frequency Fluctuation.** Using 200 000 configurations obtained from the MD trajectory, we calculated CO stretch frequency shifts for the two MbCO's, where the electric potential values  $\phi(\mathbf{R}_x)$  at twenty distributed sites were calculated with the AMBER partial charges of amino acids and water molecules. In Figures 5a and b, parts of the CO stretch frequency trajectories of wild-type and double mutant, respectively, are shown.

The vibrational frequency trajectory (Figure 5a) of the wild-type MbCO exhibits transitions between two frequency-resolved states,  $A_1$  and  $A_3$ . In Figures 5c and e, we plot the time-dependent change of His64  $C_\alpha\text{---}C_\beta\text{---}C_\gamma\text{---}C_\delta$  dihedral angle and the distance between the  $N_e$ -atom of His64 and the oxygen atom of CO, respectively. Note that the His64 can form a direct hydrogen bonding interaction with CO. As can be seen in Figures 5a, c, and e, the CO frequency of the wild-type MbCO is correlated with the dihedral angle as well as the His64 $N_e\cdots\text{OC}$  distance. Thus, in this case of the wild-type, the low frequency state corresponds to the  $A_3$  state with  $-16.5 \text{ cm}^{-1}$  frequency shift on average, whereas the high frequency state to the  $A_1$  state with  $1.4 \text{ cm}^{-1}$  frequency shift. The frequency difference between these two states is about  $17.9 \text{ cm}^{-1}$ . The conformation transition from the lower ( $A_3$ ) to higher ( $A_1$ ) frequency state accompanies an increase in His64 $N_e\cdots\text{OC}$  distance and a change of His64  $C_\alpha\text{---}C_\beta\text{---}C_\gamma\text{---}C_\delta$  dihedral angle. More specifically, as the H-atom of the

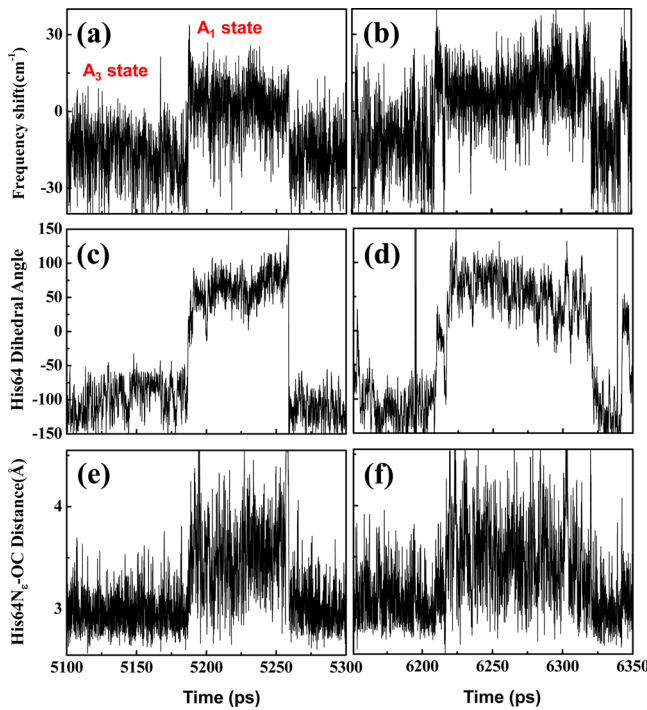


**Figure 5.** Vibrational frequency trajectories of the wild-type (a) and double mutant (b) MbCO are shown. The His64 C<sub>α</sub>—C<sub>β</sub>—C<sub>γ</sub>—C<sub>δ</sub> dihedral angles in the wild-type and double mutant MbCO's are plotted with respect to time in parts c and d. The distances between the N<sub>e</sub>-atom of His64 O and O-atom of CO in the wild-type and double mutant MbCO's are plotted with respect to time in parts e and f.

(His64)N<sub>e</sub>—H approaches to the CO oxygen atom to make an hydrogen bond, the bond strength of CO increases, and its stretching frequency is red-shifted. In fact, our simulated distance change upon transition between the A<sub>1</sub> and A<sub>3</sub> states can be directly compared with the experimental result from X-ray crystallography. Vojtechovsky et al. reported high resolution X-ray structures for distinct A<sub>1</sub> and A<sub>3</sub> wild-type MbCO conformations and found that the His64N<sub>e</sub>···OC distances are 3.2 and 2.7 Å, respectively.<sup>66</sup> The average distances estimated by using our MD trajectories are found to be 3.6 and 3.0 Å for the A<sub>1</sub> and A<sub>3</sub> states, respectively. The relative distance change by 0.6 Å upon transition from A<sub>3</sub> to A<sub>1</sub> is very close to the crystallographic result of 0.5 (= 3.2 – 2.7) Å. However, a caution is needed in this comparison, because the experimental value was obtained from crystal structures. Nonetheless, for the same protein, a similar MD simulation study was already performed by Merchant et al. and they found that the corresponding His64N<sub>e</sub>···OC distance change upon transition from A<sub>3</sub> to A<sub>1</sub> was estimated to be 1.4 Å, where they measured the distances between the His64N<sub>e</sub>-H proton and the midpoint of CO molecule instead.<sup>46</sup> It is believed that an important improvement in estimating the corresponding distance change in the present work is mainly due to the use of different force field (MOIL is replaced with AMBER) as well as to significantly increased partial charges for CO ( $\pm 0.021e$  in ref 46 are replaced with  $\pm 0.174e$ ).

We next examine the frequency shift trajectory of the double mutant MbCO (see Figure 5b), which also exhibits multiple transitions between states, though the frequency differences among them are comparatively small. Although those states of the double mutant have similar average frequency shifts, the

frequency fluctuation amplitudes are notably larger than those of the wild-type. When Figures 5c and e for the wild-type are compared with Figures 5d and f for the double mutant, the corresponding dihedral angle, and distance trajectories appear to be similar to each other, even though their fluctuation amplitudes in the case of the double mutant are comparatively large. For the wild-type, the high (low) frequency A<sub>1</sub> (A<sub>3</sub>) state has the dihedral angle of 80° (−100°) and the distance of 3.6 (3.0) Å. There is no ambiguity in assigning the two spectroscopically distinguishable states to the corresponding two imidazole ring conformations of His64. Of course, there are other structural movements involved in such conformational transitions between two states other than His64. A quick inspection of Figures 5d and f for the double mutant, which are similar to Figures 5c and e, leads to the conclusion that the previous assignment that the low and high frequency components in its IR spectrum can be similarly assigned to the A<sub>1</sub> and A<sub>3</sub> states of the wild-type.<sup>18</sup> However, there is a notable difference between the wild-type and double mutant proteins. As can be seen in Figure 5b, the corresponding frequency trajectories cannot be simply divided into two states in the case of the double mutant. Furthermore, a careful examination of the entire time-dependent dihedral angle trajectory (not just a short segment shown in Figure 5d) reveals that there are four distinct substates that are designated as A<sub>1a</sub>, A<sub>1b</sub>, A<sub>3a</sub>, and A<sub>3b</sub>. As these notations indicate, A<sub>1a</sub> and A<sub>1b</sub> are two substates having similar dihedral angles and are not easily distinguishable by means of vibrational spectroscopy due to the small frequency difference. In addition, the double mutation of MbCO seems to make the A<sub>3</sub> state of the wild-type divided into A<sub>3a</sub> and A<sub>3b</sub> substates having different dihedral angles. We shall discuss characteristic structural features of these conformational substates in the next section by considering two-dimensional PMF surfaces.

As can be inferred from Figures 5a and b, the vibrational frequency trajectories for the two proteins show *approximately* two-state behavior so that one might expect that the total frequency distribution would appear to be a doublet. In Figure 6, the instantaneous CO stretch frequency distribution of the wild-type is shown and appears to be highly asymmetric (two-Gaussian fits are also shown in Figure 6a). In contrast, that of the double mutant is quite symmetric and there appears no notable shoulder peak. This difference can be understood by noting that the fluctuation amplitude of vibrational frequency shift of the double mutant is much larger than that of the wild-type. Consequently, the frequency resolution is not observed in the double mutant case, so that the entire frequency distributions do not provide critical information about the hidden substates of the double mutant. Nevertheless, it is interesting to note that the average frequency shifts,  $\langle \Delta\omega \rangle$ , are  $-4.7$  and  $-12.1$  cm<sup>−1</sup> for the wild-type and the double mutant MbCO's, respectively. The fact that the average frequency redshift of the double mutant is much larger than that of the wild-type strongly indicates that the CO in the double mutant tends to form a stronger and more prolonged H-bond with His64. Furthermore, the observations that (i) the corresponding CO frequencies of the two major states are more or less the same for the wild-type and double mutant MbCO's and (ii) the instantaneous frequency distributions for the two are significantly different suggest that the relative populations of the involved states are quite different for the two proteins.

**C. Two-Dimensional Potential Energy Surface.** The potential energy surface (PES) provides us the details of

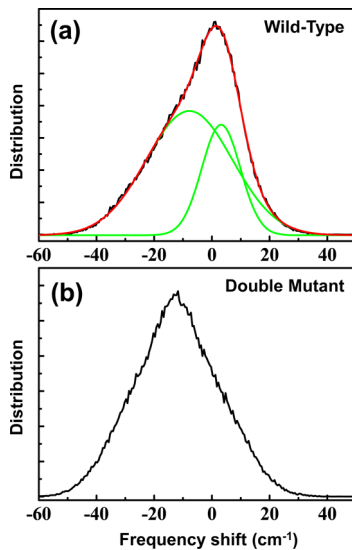


**Figure 6.** Distributions of CO stretch frequency shifts of the wild-type (a) and double mutant (b) MbCO's. The frequency shift distribution of the wild-type is fit with two Gaussian functions (see the green lines in part a). Here, the red line in part a is the fitting result.

thermodynamic and kinetic properties of chemical reactions involving a potential barrier-crossing. Although, in general, the PES is highly complicated due to its multidimensionality, it can be simplified if one can identify the best set of collective reaction coordinates to describe the overall reaction. Thus, a proper choice of reaction coordinate is always essential in identifying local minimum structures and determining barrier heights along the reaction coordinate.

For the MbCO, it is well-known that the distal histidine is the most important structural factor that governs the vibrational spectrum of CO.<sup>46</sup> The relative position of the distal histidine from the CO has been known to be directly related to the three distinctive vibrational bands ( $A_0$ ,  $A_1$ , and  $A_3$  states). Among them, the interconversion between  $A_1$  and  $A_3$  has been expected to occur in faster time scale than transition between  $A_0$  and  $A_1$  or  $A_3$  states.<sup>67</sup> On the basis of the previous works,<sup>18,44,46</sup> the characteristic factors determining the structures associated with the three states are (i) the distance  $\text{His}64\text{N}_e \cdots \text{OC}$ , (ii) the distance  $\text{His}64\text{N}_\delta \cdots \text{OC}$ , and (iii) the  $C_\alpha-C_\beta-C_\gamma-C_{\delta 2}$  dihedral angle (see Figure 1 for atomic designations) of the imidazole side-chain of His64. In fact, the potential of mean force (PMF) along these coordinates were therefore used to confirm the existence of such states and to estimate the activation energies.<sup>44</sup> As shown by Merchant et al., the three coordinates are not independent and clearly correlated with the CO frequency.<sup>46</sup>

Here, we calculated the two-dimensional (2D) PMF with respect to the two structural coordinates i and iii, because they are considered to be the most representative ones. Figure 7 depicts the 2D PMF's of the wild-type and the double mutant. One can immediately find similarity and difference between the two. First of all, the overall shapes of the two PMF surfaces are qualitatively similar, which indicates that the allowed configurations of the His64 imidazole in the heme pocket are the same even after double mutation. More specifically, there are two local minima in the wild-type PMF, which is also similar to that of the double mutant. The corresponding dihedral angles and distances for the two minima denoted as  $A_1$  and  $A_3$  are the same, which explains the similarity in the

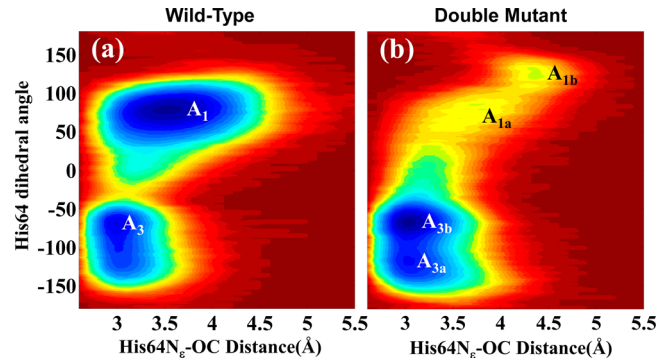


**Figure 7.** Two-dimensional potential of mean forces of the wild-type (a) and double mutant (b) MbCO's. The  $x$ - and  $y$ -axes are the  $\text{His}64\text{N}_e\cdots\text{OC}$  distance and the  $C_\alpha-C_\beta-C_\gamma-C_{\delta 2}$  dihedral angle, respectively.

frequency trajectories of the two cases (Figures 5a and b). However, there are certain and quite important differences in the two PMF surfaces.

In the case of the wild-type, there exist only two local minima separated by the dihedral angle, though the distribution of the distance  $\text{His}64\text{N}_e \cdots \text{OC}$  of the  $A_1$  state overlaps with that of  $A_3$ . To examine the possibility that the two conformational states  $A_1$  and  $A_3$  are indeed the two frequency-resolved components in the IR spectrum, we separately calculated the frequency distributions of each conformation. Here, the dividing line at the transition state between  $A_1$  and  $A_3$  is assumed to be at the dihedral angle of  $-25^\circ$  (see Figure 8a). The vibrational frequency distributions of the  $A_1$  and  $A_3$  states are plotted in Figure 8b. As expected, the  $A_3$  conformation with the dihedral angle smaller than  $-25^\circ$  produces a low-frequency peak with maximum at  $-16.5\text{ cm}^{-1}$ . This conformation is indeed associated with the structure involving a strong hydrogen bonding interaction between  $\text{His}64\text{N}_e\text{H}$  proton and CO oxygen atom. The  $A_1$  conformation with dihedral angle larger than  $-25^\circ$  is associated with the high frequency peak ( $1.4\text{ cm}^{-1}$ ) in Figure 8b, and it has weak or no hydrogen bonding interaction. This finding is consistent with the previous work.<sup>46</sup> From the 2D PMF surface in Figure 7a, one can draw a reaction pathway connecting the two local minima, which mainly involves an internal rotation along the His64 dihedral angle (see Supporting Information Figure S1). The free energy curve along this reaction coordinate is shown in Figure 8a, and the free energy difference between the two states is estimated to be  $0.24\text{ kcal/mol}$  that results in the population ratio of  $A_3$  to  $A_1$  to be  $0.66:1$ .

In the case of the double mutant, the mutation induces significant changes in the relative free energies of the local minimum structures (Figure 7b). First of all, despite the fact that the overall position of the  $A_3$  state in the 2D PMF for the double mutant is similar to that for the wild-type, it becomes split into two local minima denoted as  $A_{3a}$  ( $-180^\circ < \text{angle} < -100^\circ$ ) and  $A_{3b}$  ( $-100^\circ < \text{angle} < 45^\circ$ ) that are distinguishable by the difference in their His64 dihedral angles. Second, the  $A_1$  state in the wild-type becomes comparatively unstable upon double mutation and also there appear two substates denoted as  $A_{1a}$  and  $A_{1b}$ . Nevertheless, it is still true that the  $A_{1a} + A_{1b}$  state is clearly separated from the  $A_{3a} + A_{3b}$  state in the case of the double mutant too. The energies of the  $A_{3a}$ ,  $A_{1a}$ , and  $A_{1b}$  states are larger than that of the  $A_{3b}$  state by  $0.40$ ,  $1.97$ , and  $2.00\text{ kcal/mol}$ , respectively (see Figure 8c) Thus, we found that the

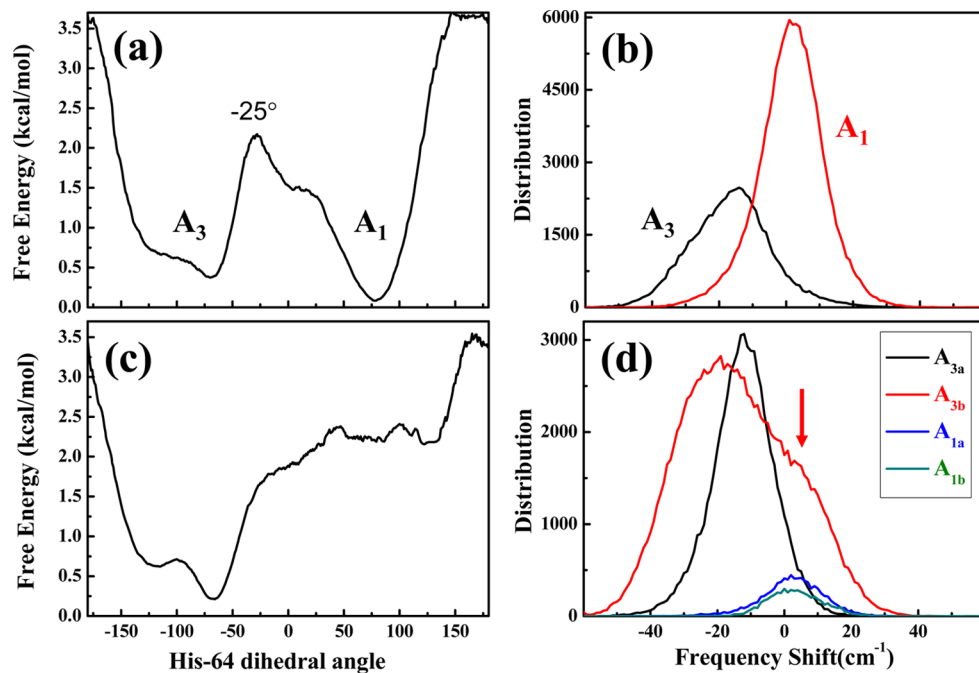


**Figure 8.** Free energy curves along the reaction pathway for the wild-type (a) and double mutant (c) MbCO. The vibrational frequency trajectories could be divided into segments associated with specific states (or substates). The vibrational frequency shift distributions of the two states A<sub>1</sub> and A<sub>3</sub> of the wild-type MbCO are plotted in part b. The vibrational frequency shift distributions of the four substates of the double mutant MbCO are shown in part d.

relative populations are estimated to be 0.51:1.0:0.04:0.03 for A<sub>3a</sub>:A<sub>3b</sub>:A<sub>1a</sub>:A<sub>1b</sub>. Here, it should be emphasized that this result on the relative populations between A<sub>1</sub> (= A<sub>1a</sub> + A<sub>1b</sub>) and A<sub>3</sub> (= A<sub>3a</sub> + A<sub>3b</sub>) states for this double mutant is quite similar to those obtained by the Voth group, even though the potential energy barrier between the two states was estimated to be significantly larger than ours.<sup>44</sup> The frequency distributions of all four substates are shown in Figure 8d. Except the A<sub>3b</sub> state, they all appear to be fairly symmetric and the average frequency shifts are -12.3, 2.2, and 3.2 cm<sup>-1</sup> for the A<sub>3a</sub>, A<sub>1a</sub>, and A<sub>1b</sub> states, respectively. It is quite interesting to note that the frequency distribution of the most populated (stable) A<sub>3b</sub> state is quite broad and even exhibits a shoulder peak in the high frequency side. This high frequency shoulder peak pointed by a red arrow in Figure 8d mainly comes from the conformations with the dihedral angle in the range from 0° to 45°. The average frequency shift (-13.9 cm<sup>-1</sup>) of the A<sub>3b</sub> state is close to that (-12.3 cm<sup>-1</sup>) of the A<sub>3a</sub> state. Due to this small frequency difference and very large frequency fluctuation amplitude of the A<sub>3b</sub> state in particular, we find it useful to group the four states into two: one with negative frequency shift (A<sub>3a</sub> + A<sub>3b</sub>) and the other with positive frequency shift (A<sub>1a</sub> + A<sub>1b</sub>). This approximate two-state description can be used to explain the appearance of a two-state behavior in the frequency trajectory (Figure 5b) and the two peaks (one major peak and a shoulder peak) in the experimental and numerically simulated IR spectra, which will be shown later in this paper.

From the 2D PMF surface of the double mutant, we find that the major dynamics of His64 are on the A<sub>3</sub> (= A<sub>3a</sub> + A<sub>3b</sub>) potential energy well, which is in stark contrast with the approximately equal populations of the A<sub>1</sub> and A<sub>3</sub> states in the case of the wild-type. More specifically, one of the important mutation-induced effects is to restrict the motion of His64 imidazole ring that is tightly bound to CO via a strong H-bonding interaction. In fact, this change in local structure

around CO in the double mutant results in a red-shifted CO stretch frequency distribution as compared to that of the wild-type (compare Figures 6a and b).

In addition to the equilibrium population ratios of all the important substates, it becomes possible to extract information about the potential energy barriers. As can be seen in Figure 8a, the energy barriers for the A<sub>3</sub> → A<sub>1</sub> and A<sub>1</sub> → A<sub>3</sub> conformational transitions are estimated to be 1.8 and 2.1 kcal/mol, respectively. In the double mutant, the barrier for A<sub>3b</sub> → A<sub>3a</sub> is as small as 0.093 kcal/mol, and those of A<sub>1a</sub> → A<sub>3a</sub> and A<sub>1b</sub> → A<sub>1a</sub> are 0.194 and 0.222 kcal/mol, respectively. Before we present the numerical simulation results on the corresponding 2D IR spectra, let us examine the possibility of chemical exchange between the two states for the wild-type. Note that, due to the frequency separation between the A<sub>1</sub> and A<sub>3</sub> states in this case, one can expect to see evidence on the chemical exchange process with a simple two state model, A<sub>1</sub> ⇌ A<sub>3</sub>. However, the double mutant has four substates so that the chemical exchange behavior is likely to be more complicated. Nevertheless, since the dihedral angle is still considered to be a good reaction coordinate, one can assume a sequential exchange dynamics among four states as A<sub>1a</sub> ⇌ A<sub>1b</sub> ⇌ A<sub>3a</sub> ⇌ A<sub>3b</sub>. Yet, it should be noted that the existence of separate substates does not guarantee that one can observe their exchange dynamics with 2D IR experiments because the 2D IR or any other vibrational spectroscopic methods require spectrally separated peaks associated with different conformations. Due to the broad and overlapping frequency distributions in the case of the double mutant (see Figure 8d), it is not clear whether there will appear any notable signature of chemical exchange dynamics in the 2D IR spectroscopy of the double mutant. Thus, using the MD and vibrational frequency trajectories, we next calculate both the IR absorption and 2D IR spectra of these two systems.

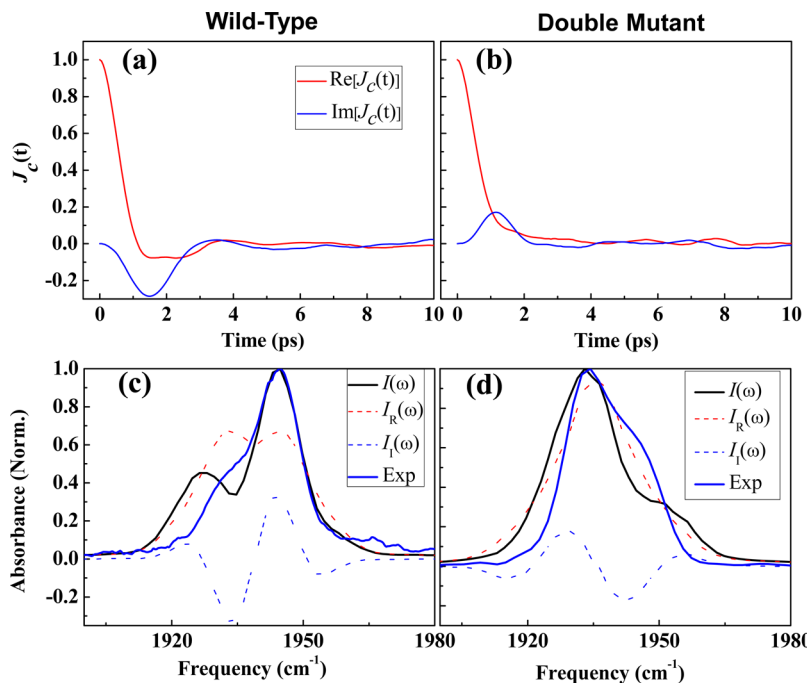


**Figure 9.** Real and imaginary parts of  $J_c(t)$  (wild-type (a) and double mutant (b)). The calculated IR spectra are plotted with the two separate contributions of  $I_R(\omega)$  and  $I_I(\omega)$  in parts c and d. Here, the experimentally measured spectra (blue solid lines in parts c and d) are also shown for the sake of comparison.

#### IV. SIMULATED IR ABSORPTION SPECTRA

As shown in Figure 6, the CO stretch frequency distributions for the wild-type and double mutant MbCO are not Gaussian. Therefore, the second-order truncated cumulant approximation method cannot be used to calculate the linear response function associated with the vibrational absorption spectrum. Thus, we here use another approach developed before, which relies on direct calculation of the linear response function. By considering the fluctuating frequency as classical function of solvent configuration, the linear response function is given approximately as<sup>88–90</sup>

$$J_c(t) = \langle \exp[-i \int_0^t d\tau \delta\omega_{10}(\mathbf{p}(\tau), \mathbf{q}(\tau))] \rangle \quad (5)$$

where the fluctuating part of the CO stretch mode frequency is denoted as  $\delta\omega_{10}(\tau)$  ( $= \omega_{10}(\tau) - \langle \omega_{10} \rangle$ ). The angle bracket in eq 5 is to take an ensemble average of the exponential function. Then, the calculated real and imaginary parts of  $J_c(t)$ 's associated with the wild-type and the double mutant are plotted in Figure 9a and b, respectively. The real parts of  $J_c(t)$  for the two proteins are similar to each other, while the imaginary parts display opposite sign within the 2 ps time window. Then, by carrying out the Fourier transformation of  $J_c(t)$ , one can obtain the IR absorption spectrum, i.e.,<sup>88</sup>

$$I(\omega) = I_R(\omega) + I_I(\omega)$$

where  $I_R(\omega)$  and  $I_I(\omega)$  are defined as

$$\begin{aligned} I_R(\omega) &= \int_0^\infty dt \cos\{(\omega - \langle \omega_{10} \rangle)t\} \text{Re}[J_c(t)] \\ I_I(\omega) &= - \int_0^\infty dt \sin\{(\omega - \langle \omega_{10} \rangle)t\} \text{Im}[J_c(t)] \end{aligned} \quad (6)$$

Here, the vibrational population relaxation is treated in an ad hoc manner by replacing  $J_c(t)$  with  $J_c(t)\exp(-t/2T_1)$ , where  $T_1$

is the average vibrational lifetime. Since the experimentally measured lifetimes are 22 and 20 ps for  $A_1$  and  $A_3$  in the case of the double mutant, we used  $T_1 = 21$  ps for the double mutant.<sup>18</sup> The lifetimes of the  $A_1$  and  $A_3$  states of the wild-type were measured to be 16.5 and 14.7 ps, respectively, so that for the present numerical simulation,  $T_1$  is assumed to be 15.6 ps.<sup>46</sup> In both proteins, the  $A_3$  state seems to have slightly shorter lifetime. Perhaps, this can be explained by noting that the  $A_3$  state involves a strong H-bonding interaction with the distal His64, which serves as an effective intermolecular vibrational energy relaxation channel. In addition, the hydrogen bonding interaction in the  $A_3$  state, which causes the redshift of CO frequency, may affect the strength of  $d-\pi^*$  back bonding interaction between Fe and CO, which could also cause a faster intramolecular relaxation of CO vibrational energy.<sup>91–93</sup>

The IR absorption spectra of the wild-type and double mutant MbCO's are shown in Figure 9c and d, respectively. The IR spectrum of the wild-type clearly shows frequency-resolved doublet feature, even though the instantaneous frequency distribution was found to be broad with a weak shoulder in the low frequency side (see Figure 6a). This is the well-known motional narrowing effect. Furthermore, despite the fact that the instantaneous frequency distribution of the double mutant appeared to be a symmetric singlet (see Figure 6b), the numerically simulated IR spectrum (black line) in Figure 9d displays a notable shoulder band on the high frequency region. Note that the frequency separation in each IR spectrum is related to the oscillatory feature in the  $\text{Re}[J_c(t)]$  function and the dispersive shape of the spectrum is to the sign of the  $\text{Im}[J_c(t)]$  function. To further test the validity of the present computational method and results, we directly compare our simulated IR spectra with the experimentally measured ones (the blue line in Figure 9c and d). The IR spectra obtained by using the ensemble averaging method are in good agreement with those obtained by the Fayer group.<sup>18,46</sup> Strictly

speaking, there are however some discrepancies between theory and experiment in the IR absorption spectra. Especially, the  $A_1$  and  $A_3$  peak positions as well as bandwidths are slightly different from the experimental results of wild type and double mutant. Such quantitative disagreement may originate from the incomplete transferability of the semiempirical map developed here for describing vibrational frequency shift. Note that the map was obtained by carrying out quantum chemistry calculations for a number of cluster systems consisting of heme–CO and amino-acid-mimicking compounds with water. Perhaps, the molecular structures and atomic charges of heme-bound CO and model compounds considered are likely to be different from those in the MD simulations. To overcome this difficulty, a QM/MM MD simulation method with high quality basis sets for the QM part will be of use.

The simulated IR spectrum of the wild-type shows two separate peaks with peak-to-peak frequency difference of  $18\text{ cm}^{-1}$ , which is comparable to the experimental value of  $11\text{ cm}^{-1}$ . Recently, Merchant et al. predicted the peak splitting to be about  $19\text{ cm}^{-1}$  using the vibrational Stark tuning rate treated as an adjustable parameter to fit the vibrational echo spectrum.<sup>46</sup> Here, it should be emphasized we did not have to use any adjustable parameters to reproduce the IR absorption spectra. Here, we already calculated the population ratio of the two states,  $A_3/A_1 = 0.66$ , using the 2D PMF surface. Now, it is assumed that the relative areas of the two peaks are proportional to their relative concentration. That is to say, the dipole strengths of the CO stretch modes in the two states are assumed to be the same. Then, one can make a fit to the experimentally measured and numerically simulated IR spectra with two Gaussian functions (see Supporting Information Figure S2). The experimentally determined population ratio (0.46 for  $A_3/A_1$ ) obtained from fitting the IR spectrum is almost the same as that from the simulated IR spectrum (0.45)—note that, due to the difference of the line-broadenings of the two states, the population ratio obtained from fitting can be different from that purely based on free energy difference between the two states. Hereafter, for the sake of direct comparisons with the experimental results reported before, we shall use the population ratio (0.45) determined from the fitting analysis of the simulated IR spectrum.

The numerically simulated IR spectrum of the double mutant is also quite similar to the experimental one (Figure 9d), though the relative intensity of the shoulder peak in the simulated spectrum is relatively smaller and more blue-shifted than that in the experimental spectrum. Over the years, three different MbCO's have been studied with 2D-IR: wild-type, single mutant L29I, and double mutant T67R/S92D.<sup>18,46,61</sup> It was shown that upon site-directed mutation the  $A_3$  IR band intensity increases but its peak position remains the same. This implies that the local environment around CO is not significantly changed, but the relative free energy of the  $A_3$  state is lowered. Indeed, our 2D PMF surface supports this interpretation. Although we identified four substates in the 2D PMF of the double mutant, due to little frequency differences between  $A_{1a}$  and  $A_{1b}$  and between  $A_{3a}$  and  $A_{3b}$ , the simulated IR spectrum can be fit with two components with frequency separation of  $20\text{ cm}^{-1}$ , which is a bit larger than the experimentally measured values, and the population ratio is found to be 1:0.17—note that the ratio obtained from the fitting analysis of the experimental spectrum is 1:0.75. Such two-component fitting to the IR absorption spectrum of the

double mutant is important because it enables us to analyze the 2D IR spectra by using a simple two-state kinetic model.

Using the vibrational frequency trajectory, we calculated the equilibrium frequency–frequency correlation function (FFCF) defined as

$$C(t) = \langle \delta\omega(t)\delta\omega(0) \rangle \quad (7)$$

Although the FFCF cannot be used to calculate the linear and nonlinear IR signal because of the non-Gaussian shape of the corresponding frequency distribution, it can still be compared with the experimental results derived from the spectral diffusion analysis of the experimentally measured 2D IR spectra. The conventional cumulant approach using the frequency–frequency correlation functions of the two states,  $A_1$  and  $A_3$ , would be applicable if the two states are frequency-resolved and they have sufficiently long lifetimes with slow interconversion rates. Perhaps, the wild-type MbCO system satisfies this condition so that the FFCF's of the two states would be sufficient enough to simulate the corresponding linear and nonlinear spectra. In that case, the resulting spectra are just the sum of the two. However, due to rapid interconversion processes between states of the double mutant, the direct ensemble-averaging methods for calculating linear and nonlinear vibrational response functions, which are used here in this paper, would be more useful than the conventional cumulant approach.

In Figure 10, the normalized FFCF's of the wild-type and double mutant MbCO's are plotted. The black lines in this

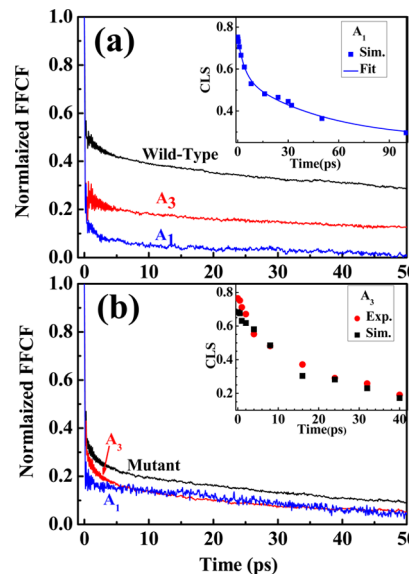


**Figure 10.** Frequency–frequency correlation functions: (a) wild-type MbCO and (b) double mutant MbCO. The CLS (center-line-slope) values of the  $A_1$  state of the wild-type as well as the  $A_3$  state of the double mutant, which are extracted from the simulated 2D IR spectra, are presented in the insets. In particular, the CLS values of the  $A_3$  state of the double mutant are directly compared with the experimental results reported by the Fayer group (see the main text for detailed discussion).

figure represent the FFCF calculated by using the entire frequency shift trajectory without separately considering different states. A notable difference in the decay pattern of the FFCF's of the two proteins is that the FFCF of the wild-type decays much slower than the double mutant—note that

**Table 1.** Fitting Parameters for Frequency–Frequency Correlation Functions<sup>a</sup>

	$\Delta_1$ (cm <sup>-1</sup> )	$\tau_1$ (ps)	$\Delta_2$ (cm <sup>-1</sup> )	$\tau_2$ (ps)	$\Delta_3$ (cm <sup>-1</sup> )	$\tau_3$ (ps)
WT A <sub>1</sub>	11.1	0.06	4.2 (2.2)	1.4 (4)	3.3 (3.2)	32.2 (32)
WT A <sub>3</sub>	8.8	0.06	2.5	4.4	4.4	117
DM A <sub>1</sub>	7.9	0.05	NA (2.7)	NA (2.5)	3.7 (4.1)	40.0 (34)
DM A <sub>3</sub>	12.0	0.07	5.7(2.6)	2.1(3.3)	6.0(3.9)	40.2(39)

<sup>a</sup>Here, WT and DM represent the wild-type MbCO and the double mutant MbCO, respectively. The numbers in the parentheses are experimental results taken from ref 18.

the asymptotic value of the wild-type FFCF at 50 ps is much larger than that of the double mutant. This can be easily explained by noting that there is a slow dynamic component associated with conformational transitions between the A<sub>1</sub> and A<sub>3</sub> states. Now, for direct comparisons with the experimental results, the entire frequency trajectory is divided into two trajectories of the A<sub>1</sub> and A<sub>3</sub> states. In the case of the double mutant, if the His64 dihedral angle is smaller (larger) than 45°, the corresponding trajectory is assigned to the A<sub>3</sub> (A<sub>1</sub>) state. The resulting FFCFs are plotted in Figure 10.

The FFCF of the wild-type A<sub>3</sub> state decays slower than that of A<sub>1</sub>, which is due to the fact that the PES of the A<sub>3</sub> state is shallow and broad as compared to that of the A<sub>1</sub> state. In contrast, the FFCF's of the two states of the double mutant exhibit similar decaying patterns. For quantitative comparisons with experiments, all the FFCFs are fit with a triexponential function

$$C(t) = \Delta_1^2 \exp(-t/\tau_1) + \Delta_2^2 \exp(-t/\tau_2) + \Delta_3^2 \exp(-t/\tau_3) \quad (8)$$

Except for the FFCF of the double mutant A<sub>1</sub> state, at least three exponential components were needed to fit to all the other FFCF's (see Supporting Information Figure S3). The fitting results on the amplitude and correlation time of each exponential component are summarized in Table 1. The first (rapidly decaying) exponential component of the FFCF's are in the motional narrowing limit, that is to say,  $\Delta_1\tau_1 < 1$ , whereas the slower components are not. The amplitudes and correlation times of the fast and slow components are now compared with the experimental values and found to be quite similar to the experimental results, though we could not observe the fast decaying component in the double mutant A<sub>1</sub> state.<sup>18</sup> This quantitative agreement of the simulated spectral diffusion dynamics with experimental results implies that the present MD simulations do reflect the dynamic behavior of the wild-type and double mutant MbCO's. Furthermore, this suggests that the two-state analysis even for the double mutant is a reasonable approach to further analyzing the time-resolved 2D IR data. In fact, one of the most stringent tests of the present computational and simulation studies of MbCO systems is to predict the 2D IR spectra and to directly compare them with the experimental data.

## V. SIMULATED 2D IR SPECTRA

As described in section IV, the ensemble averaging method for calculating the linear response function was successful so that the same method is used to simulate the 2D IR photon echo spectra. As shown in ref 88, the nonlinear response functions contributing to the photon echo signal are given as

$$\begin{aligned} \Phi_1(t_3, t_2, t_1) &= -|\mu_{01}|^2 |\mu_{12}|^2 \exp\{-i\langle\omega_{21}\rangle t_3 + i\langle\omega_{10}\rangle t_1\} \Psi_A \\ &\quad (t_3, t_2, t_1) \Gamma_{TA}(t_3, t_2, t_1) \\ \Phi_2(t_3, t_2, t_1) &= -|\mu_{01}|^2 |\mu_{12}|^2 \exp\{-i\langle\omega_{21}\rangle t_3 - i\langle\omega_{10}\rangle t_1\} \Psi_B \\ &\quad (t_3, t_2, t_1) \Gamma_{TA}(t_3, t_2, t_1) \\ \Phi_3(t_3, t_2, t_1) &= -|\mu_{01}|^4 \exp\{-i\langle\omega_{10}\rangle t_3 + i\langle\omega_{10}\rangle t_1\} \Psi_A \\ &\quad (t_3, t_2, t_1) \Gamma_{SE}(t_3, t_2, t_1) \\ \Phi_4(t_3, t_2, t_1) &= -|\mu_{01}|^4 \exp\{-i\langle\omega_{10}\rangle t_3 - i\langle\omega_{10}\rangle t_1\} \Psi_B \\ &\quad (t_3, t_2, t_1) \Gamma_{SE}(t_3, t_2, t_1) \\ \Phi_5(t_3, t_2, t_1) &= -|\mu_{01}|^4 \exp\{-i\langle\omega_{10}\rangle t_3 + i\langle\omega_{10}\rangle t_1\} \Psi_A \\ &\quad (t_3, t_2, t_1) \Gamma_{GB}(t_3, t_2, t_1) \\ \Phi_6(t_3, t_2, t_1) &= -|\mu_{01}|^4 \exp\{-i\langle\omega_{10}\rangle t_3 - i\langle\omega_{10}\rangle t_1\} \Psi_B \\ &\quad (t_3, t_2, t_1) \Gamma_{GB}(t_3, t_2, t_1) \end{aligned} \quad (9)$$

where the dephasing-induced line broadening terms are

$$\begin{aligned} \Psi_A(t_3, t_2, t_1) &= \langle \exp\{i \int_0^{t_1} d\tau \delta\omega_{10}(\tau)\} \\ &\quad \times \exp\{-i \int_{t_1+t_2}^{t_1+t_2+t_3} d\tau \delta\omega_{10}(\tau)\} \rangle \\ \Psi_B(t_3, t_2, t_1) &= \langle \exp\{-i \int_0^{t_1} d\tau \delta\omega_{10}(\tau)\} \\ &\quad \times \exp\{-i \int_{t_1+t_2}^{t_1+t_2+t_3} d\tau \delta\omega_{10}(\tau)\} \rangle \end{aligned} \quad (10)$$

Here, the first two terms in eq 9 are associated with the transient absorption (TA), the second two terms with the simulated emission (SE), and the last two terms with the ground-state bleach (GB), respectively. The vibrational relaxation effects on the 2D IR photon echo spectrum are described by  $\Gamma(t_3, t_2, t_1)$  functions defined as

$$\begin{aligned} \Gamma_{TA}(t_3, t_2, t_1) &= \exp\left\{-\frac{(\gamma_1 + \gamma_2)t_3}{2} - \gamma_1 t_2 - \frac{\gamma_1 t_1}{2}\right\} \\ \Gamma_{SE}(t_3, t_2, t_1) &= \exp\left\{-\frac{\gamma_1 t_3}{2} - \gamma_1 t_2 - \frac{\gamma_1 t_1}{2}\right\} \\ \Gamma_{GB}(t_3, t_2, t_1) &= \exp\left\{-\frac{\gamma_1 t_3}{2} - \gamma_1 t_2 - \frac{\gamma_1 t_1}{2}\right\} \end{aligned} \quad (11)$$

The lifetimes are denoted as,  $1/\gamma_1$  and  $1/\gamma_2$ , and they were measured with polarization-controlled pump–probe spectroscopy. Once the line-broadening functions  $\Psi_A(t_3, t_2, t_1)$  and  $\Psi_B(t_3, t_2, t_1)$  are calculated using the frequency trajectories, one can obtain the 2D IR photon echo spectra for varying waiting time  $T_w$ :

$$\begin{aligned}\tilde{\Phi}_j(\omega_{\text{pr}}, \omega_{\text{pu}}; T_w) &= \int_0^\infty dt_3 \int_0^\infty dt_1 \exp\{i\omega_{\text{pr}}t_3 - i\omega_{\text{pu}}t_1\} \\ \Phi_j(t_3, t_2 = T_w, t_1), (j = 1, 3, 5)\end{aligned}$$

$$\begin{aligned}\tilde{\Phi}_k(\omega_{\text{pr}}, \omega_{\text{pu}}; T_w) &= \int_0^\infty dt_3 \int_0^\infty dt_1 \exp\{i\omega_{\text{pr}}t_3 + i\omega_{\text{pu}}t_1\} \\ \Phi_k(t_3, t_2 = T_w, t_1), (k = 2, 4, 6)\end{aligned}\quad (12)$$

Then, the 2D IR spectrum is finally given as the sum of six spectra

$$S_{2D}(\omega_{\text{pr}}, \omega_{\text{pu}}; T_w) \propto \text{Re}[\sum_{i=1}^6 \tilde{\Phi}_i(\omega_{\text{pr}}, \omega_{\text{pu}}; T_w)] \quad (13)$$

Figure 11 depicts the calculated 2D IR spectra. The diagonal peaks in the 2D IR spectra for both cases appear to be significantly elongated due to the slow components in the FFCFs.

In the case of the wild type, there are two frequency resolved diagonal peaks in the 2D IR spectra, which are associated with

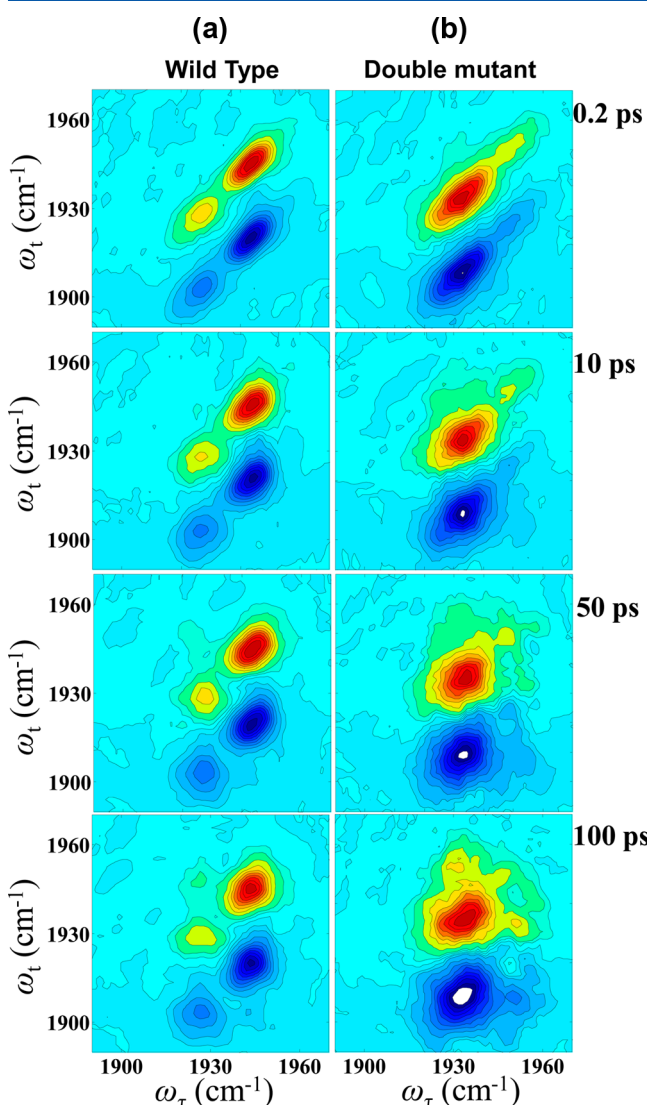


**Figure 11.** Numerically calculated 2D IR photon echo spectra for varying waiting time  $\tau$  at 0, 30, 50, and 100 ps: (a) wild-type MbCO and (b) double mutant MbCO.

the  $A_1$  and  $A_3$  states. At a short waiting time, there is no signature for the cross peaks. After 50 ps, weak cross peaks become observable in the simulated spectra. However, in real experiments, due to the small signal-to-noise ratio, it was not possible to observe the 2D IR signals at longer waiting times ( $>50$  ps). Thus, the corresponding cross peaks were not observed in the experimental spectra in refs 46 and 94, a finding which seems to be well reproduced by the present simulation results.

On the other hand, the 2D IR spectra of the double mutant exhibit weak cross peaks even at short waiting times. For instance, in the 2D IR spectrum at 10 ps, due to the increased cross peaks, the 2D line-shape in the 0–1 transition (positive signal) region looks like a right triangle because of the destructive interference of the lower-right 0–1 cross peak with the negative 1–2 diagonal of the high frequency component. At the waiting time of 50 ps, the cross peaks gain enough amplitude to overcome the small negative diagonal peak so that the square feature in the 0–1 transition region becomes clear. At 100 ps, the cross peak amplitude is even larger than the high-frequency diagonal peak—note that there appear to be two positive cross peaks.

In addition to the cross peaks, the time-dependent line-shape changes of the diagonal peaks can be compared with experimental results. In Table 1, we already compared the simulated FFCFs with the experimentally determined ones, which were obtained from the CLS (center-line-slope) method. For a more direct comparison with experiment, we also calculated the CLS values from the simulated 2D-IR spectra. When a short-time approximation to the nonlinear vibrational response function is made, one can show that the  $T_w$ -dependent CLS is proportional to FFCF.<sup>95,96</sup> However, the CLS values cannot be accurately estimated for spectrally overlapping diagonal and cross-peaks.<sup>97</sup> Therefore, among the two diagonal peaks, the more intense one is mainly analyzed here. The resulting CLS values are plotted in Figure 10 and fit with a biexponential function with a static offset (see the insets of Figure 10). In the case of the  $A_1$  diagonal peak of the wild-type, the two decay time constants are 4 and 50 ps and experimentally determined values are 4 and 32 ps.<sup>18</sup> In the case of the  $A_3$  diagonal peak of the double mutant, our CLS values extracted from the simulated 2D IR spectrum of the double mutant are quantitatively compared with the experimentally determined CLS values (see the inset of Figure 10b). Our CLS values agree well with the experimental results. Although the simulated 2D IR spectra of the double mutant are not in perfect and quantitative agreement with the experimentally measured ones in ref 18, the general spectral features and time-dependent evolutions of the 2D line-shapes are reproduced very well through the present simulation except the population ratio between the  $A_1$  and  $A_3$  states.

## VI. TWO-STATE ANALYSIS OF SIMULATED 2D IR SPECTRA

Currently available 2D IR experimental results were interpreted using a spectroscopic two-state model, where the frequency-resolved peaks were assigned to two different conformations. An important consensus emerged from those studies is that the interaction between the His64N<sub>e</sub>H proton and the CO oxygen atom via a hydrogen bond is important and it causes a red-shift in the vibrational frequency of the bound CO ligand relative to that of the  $A_0$  state. However, the precise structures associated with the vibrational spectroscopically distinguishable  $A_1$  and  $A_3$

states have not been fully understood. Irrespective of the controversy about such assignment, it was possible to analyze the 2D IR data with the spectroscopic  $A_1$  and  $A_3$  states. In this paper, we follow exactly the same procedure. That is to say, considering the numerically calculated 2D IR spectra and applying the two-state analysis method, we were able to extract the conformational transition rate between the two states. As discussed above and shown in Supporting Information Figure S2, the simulated IR spectra of the double mutant and the wild-type could be decomposed into two separate peaks.

When we carried out numerical fitting analyses of the simulated 2D IR spectra, only the 0–1 transition peaks were taken into consideration to avoid any possible complexity caused by cancellation between the positive and negative contributions. Each snapshot 2D IR spectrum was fit with tilted 2D Gaussian functions.<sup>98</sup> Thus determined volumes of the diagonal and cross peaks with respect to waiting time are plotted in Figure 12. A simple two-state kinetic model was successfully used to fit these waiting time-dependent volume changes, where the exchange rate is the only fitting parameter.

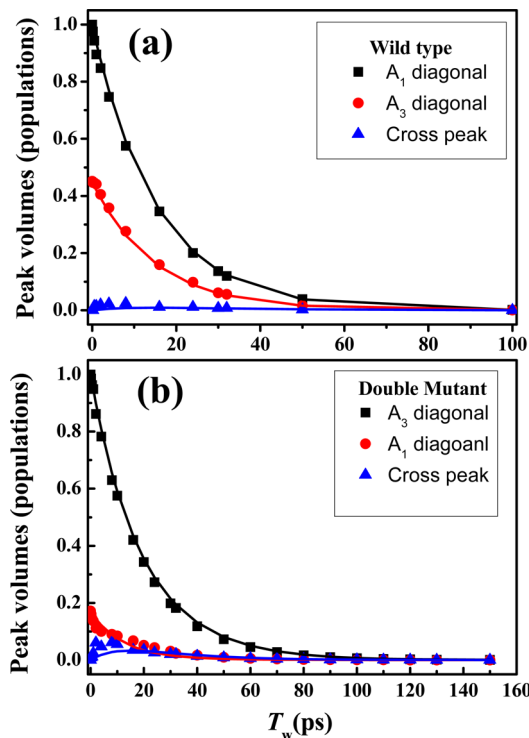


**Figure 12.** Peak volumes obtained from the numerically calculated 2D IR spectra (in Figure 11) for (a) wild-type and (b) double mutant MbCO's. Here, a two-dimensional tilted Gaussian function was used to carry out volume fittings to both diagonal and cross peaks.

In the case of the wild-type, all the derived volumes in Figure 12a are fit well with the exchange time of 278 ps. This corresponds to the time constant associated with the conformational transition from  $A_3$  to  $A_1$  states. Considering the short lifetime of the  $A_1$  and  $A_3$  states of the wild-type, it is understandable that the cross peak could not be observed in the experimentally measured spectra before, but the present simulated 2D IR spectroscopy can be extended to 100 ps so that the cross peak becomes observable. In the case of the double mutant, we found that the exchange time is 28 ps, which is comparable to the experimentally measured lifetimes of the

two states. Again this exchange time for the double mutant corresponds to the conformational transition from  $A_1$  ( $= A_{1a} + A_{1b}$ ) to  $A_3$  ( $= A_{3a} + A_{3b}$ ). Our estimated exchange time of 28 ps is comparatively shorter than the experimental result (76 ps) reported by the Fayer group,<sup>18</sup> but still the genuine 2D spectral features are nicely reproduced in the present computational results shown in Figure 11.

## VII. COMPARISONS WITH PREVIOUS WORKS

The essential goal of various spectroscopic studies of wild-type and mutant MbCO proteins is to understand how structural variations induced by site-directed mutation affect on the ligand-binding and dissociation dynamics, enzymatic activity, and dynamics and time scales of local electrostatic environment inside the heme pocket. In this regard, the 2D IR spectroscopy could be one of the most incisive tools for such investigations. The Fayer group has carried out extensive 2D IR studies of not only wild-type but also mutant MbCO's, e.g., H64V, L29I, and T67R/S92D. In particular, they found that the experimentally measured exchange rates between two spectroscopically distinguishable states are  $47 \pm 8$  and  $76 \pm 10$  ps for the single and double mutants, L29I and T67R/S92D, respectively.<sup>18,61</sup> In the case of the H64V mutant, however, the polar distal histidine was replaced by nonpolar valine and the H64V spectrum appears to be a singlet without any shoulder band. It was shown in ref 99 that the vibrational dephasing rate of CO in this mutant is significantly reduced relative to the native protein. From their MD simulation studies on the H64V, they found that the corresponding frequency–frequency correlation function is similar to that of the wild-type  $A_1$  state. Thus, it was confirmed that the distal histidine indeed plays a decisive role in determining CO vibrational dephasing and separating the  $A_1$  and  $A_3$  states. Although it would be interesting to simulate the linear and nonlinear IR spectra of the H64V by using the MD simulation method with the same set of vibrational solvatochromic parameters developed here, we have focused on the wild type and double mutant proteins in this paper. Despite those experimental studies, it should be emphasized that measuring such chemical exchange rates between two spectroscopically distinguishable states does not directly provide information on the associated structure and dynamics of the corresponding states.

One of the most interesting and directly relevant studies was performed by Bagchi et al.<sup>44</sup> Using the CHARMM software package with the CHARMM22 force field, they obtained the PMF surfaces of the single and double mutants with respect to the  $N_\delta-O$  distance. They found two minima with relative small energy barriers in the case of the L29I, whereas there is one minimum-energy structure in the case of the T67R/S92D (see Figure 5 in ref 44). Thus, the experimentally measured chemical exchange for the L29I was assigned to the conformational switching between the two states. However, since their free energy curve for the double mutant has no potential barrier separating two states, the experimentally measured chemical exchange could not be explained using their MD simulation results. They thus concluded that “either the force field is in error or the true potential energy landscape for the double mutant cannot be simply described by a simple reaction coordinate.”<sup>44</sup>

In the present work, we however found that there exists a barrier between the  $A_1$  and  $A_3$  states even in the case of the double mutant. Furthermore, directly comparing the simulated 2D IR spectra with the experimental results, we showed that the

dynamical transitions between the two states are indeed related to the experimentally observed chemical exchange. Nonetheless, it should be emphasized that the overall free energy surface for the double mutant, which was obtained by Bagchi et al.,<sup>44</sup> is quite similar to our surface except for a small energy barrier along the  $C_\alpha-C_\beta-C_\gamma-C_{\delta 2}$  dihedral angle relating to the rotation of imidazole ring. Thus, we believe that the double mutant MbCO MD trajectories obtained by Bagchi et al. are not completely incorrect at all, but, due to a lack of computational schemes for calculating CO frequency shift accurately, they were not able to simulate the 2D IR spectra that could be directly compared with the experimental results.

Now, let us address possible enhancement effects of double mutation on its peroxidase catalytic activity. Unlike the wild-type or single mutant (L29I) myoglobin, the double mutant T67R/S92D was known to have an enhanced peroxidase catalytic activity.<sup>10</sup> Apparently, such change of enzyme activity should be related to mutation-induced equilibrium structural changes in the heme pocket. On the basis of the success of simulating the linear and nonlinear vibrational spectra of the wild-type and the double mutant here, it might be possible to elucidate the characteristic structural differences between the wild-type and the double mutant. It was already known that the distal histidine His64 plays an important role in  $H_2O_2$  binding and activation processes for both wild-type and mutants.<sup>1,4,10</sup> Our MD trajectories and 2D PMF surfaces suggest that the rotation of His64 imidazole ring is restricted on the region around the  $C_\alpha-C_\beta-C_\gamma-C_{\delta 2}$  dihedral angle of  $100^\circ$  and suppresses the population of  $A_1$  state as compared to the wild-type. Furthermore, the conventional  $A_3$  state found in the wild-type consists of two local minimum structures denoted as  $A_{3a}$  and  $A_{3b}$  substates in the case of the double mutant—note that they are different from each other by the  $C_\alpha-C_\beta-C_\gamma-C_{\delta 2}$  dihedral angle. In Figure 13, the zoom-in structures of the two substates ( $A_{3a}$  and  $A_{3b}$ ) of the double mutant are shown to highlight the structural difference between the two. The bound CO is located at the center of each figure, and it is surrounded by three nonpolar amino-acid side-chains from Leu29, Phe43, and Val68. The  $A_{3a}$  structure shows a strong H-bonding interaction between His64N<sub>e</sub>H with O(CO) atom. In contrast, the  $A_{3b}$  structure involves a rotation of the His64 imidazole ring (with dihedral angle of  $-120^\circ$ ) in comparison to the  $A_{3a}$  structure and the CO molecule becomes slightly realigned to be more perpendicular to the heme plane. Nonetheless, these two substates have quite similar energies (see Figure 7), and they are highly populated in the double mutant. Since the His64N<sub>e</sub>···OC distances in these substate structures are significantly shorter than the conventional  $A_1$  state in the wild-type or  $A_{1a}$  and  $A_{1b}$  states in the double mutant, we suggest that the His64 could actively participate in the binding of peroxide and lowering activation energy along the peroxidation reaction in the case of Mb– $H_2O_2$  complex.

## VIII. SUMMARY

In this work, we developed a distributed solvatochromic charge model for quantitatively describing vibrational frequency shifts of CO stretch modes for both wild-type and double mutant MbCO systems. Then, carrying out extensive classical MD simulations for both proteins, we obtained the corresponding CO frequency trajectories and found that the instantaneous frequency distributions are highly non-Gaussian. Thus, by directly calculating the linear and nonlinear response functions using ensemble averaging method, the IR absorption and 2D IR

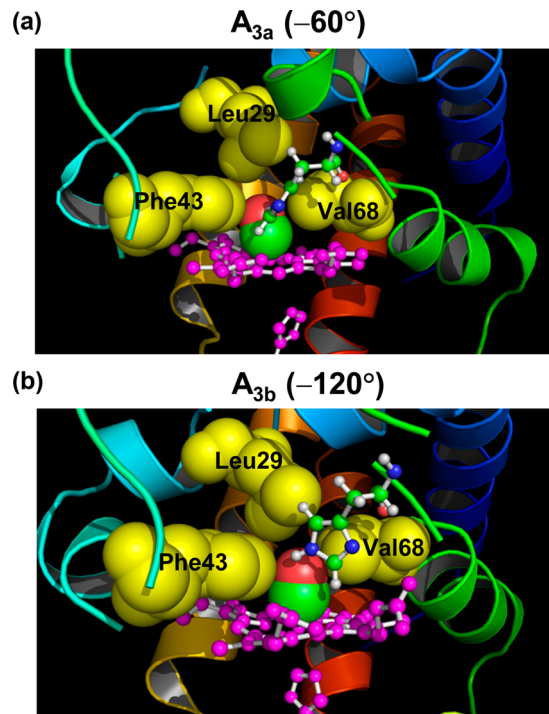


**Figure 13.** Snapshot structures of the  $A_{3a}$  (a) and  $A_{3b}$  (b) substates of the double mutant MbCO. Note that the corresponding  $C_\alpha-C_\beta-C_\gamma-C_{\delta 2}$  dihedral angles are  $-60$  and  $-120^\circ$ . In addition to the distal histidine His64, three nonpolar residues of Leu29, Phe43, and Val68 are shown here with the space-filling model.

spectra were numerically simulated and compared with the experimental results reported by the Fayer group.<sup>18,46</sup> The agreement was found to be reasonably quantitative. Furthermore using the calculated 2D PMF surfaces, we were able to directly assign the vibrational peaks to specific conformations. The reaction coordinate consisting of the His64N<sub>e</sub>···O distance and the  $C_\alpha-C_\beta-C_\gamma-C_{\delta 2}$  dihedral angle of the imidazole ring of His64 was found to be reasonable. Although, in the case of the wild-type, there are two states that are energetically and spectroscopically well-resolved, we found four different substates in the case of the double mutant. However, it was noted that, due to a lack of clear frequency resolutions among those substates, the vibrational spectroscopy cannot distinguish them. Thus, we used the same two-state kinetic model to numerically analyze the simulated IR absorption and 2D IR spectra of the two MbCO and estimated the chemical exchange times. Not only the overall time-dependence of the 2D IR spectrum but also the fitted chemical exchange time constants are in good agreement with the experimental results. Motivated by this success in simulating the highly complicated 2D IR spectra, we suggested that the potential double mutation effects on the enhanced peroxidase catalytic activity of the double mutant originate from (i) suppression of the  $A_1$  population and (ii) enhanced participation of the His64 imidazole in forming H-bonding interaction with ligand. We believe that such direct comparisons between computational IR and 2DIR spectra and experiments is one of the most stringent ways to examine the accuracy of classical force field MD simulation methods. Encouraged by the present success, we shall further investigate other types of protein mutants and establish the relationships among mutation-induced structural variations, alternation in

protein functions, and linear and nonlinear vibrational spectroscopic signals.

## ■ ASSOCIATED CONTENT

### S Supporting Information

Reaction pathways drawn on the calculated 2D potential of mean force surfaces, the fitting results of various IR spectrum, and frequency–frequency correlation functions. This material is available free of charge via the Internet at <http://pubs.acs.org>.

## ■ AUTHOR INFORMATION

### Corresponding Author

\*E-mail: mcho@korea.ac.kr (M.C.) or kkwak@cau.ac.kr (K.-W.K.). Fax: +82-2-3290-3121. Tel.: +82-2-3290-3133.

### Notes

The authors declare no competing financial interest.

## ■ ACKNOWLEDGMENTS

This work was supported by the National Research Foundation of Korea (NRF) grants funded by the Korea government (MEST) (No.: 20090078897 and 20110020033) to M.C. K.W.K. thanks the NRF fund (No.:2009-0093817) for financial support. J.H.C. thanks the Korea University Grant for financial support.

## ■ REFERENCES

- (1) Ozaki, S.-i.; Roach, M. P.; Matsui, T.; Watanabe, Y. Investigations of the Roles of the Distal Heme Environment and the Proximal Heme Iron Ligand in Peroxide Activation by Heme Enzymes via Molecular Engineering of Myoglobin. *Acc. Chem. Res.* **2001**, *34*, 818–825.
- (2) Ozaki, S.-i.; Matsui, T.; Watanabe, Y. Conversion of Myoglobin into a Highly Stereo-specific Peroxygenase by the L29H/H64L Mutation. *J. Am. Chem. Soc.* **1996**, *118*, 9784–9785.
- (3) Ozaki, S.-i.; Matsui, T.; Watanabe, Y. Conversion of Myoglobin into a Peroxygenase: A Catalytic Intermediate of Sulfoxidation and Epoxidation by the F43H/H64L Mutant. *J. Am. Chem. Soc.* **1997**, *119*, 6666–6667.
- (4) Matsui, T.; Ozaki, S.-i.; Liong, E.; Phillips, G. N.; Watanabe, Y. Effects of the Location of Distal Histidine in the Reaction of Myoglobin with Hydrogen Peroxide. *J. Biol. Chem.* **1999**, *274*, 2838–2844.
- (5) Redaelli, C.; Monzani, E.; Santagostini, L.; Casella, L.; Sanangeltoni, A. M.; Pierattelli, R.; Banci, L. Characterization and Peroxidase Activity of a Myoglobin Mutant Containing a Distal Arginine. *ChemBioChem* **2002**, *3*, 226–233.
- (6) Frauenfelder, H.; McMahon, B. H.; Austin, R. H.; Chu, K.; Groves, J. T. The Role of Structure, Energy Landscape, Dynamics, and Allostery in the Enzymatic Function of Myoglobin. *Proc. Natl. Acad. Sci. U.S.A.* **2001**, *98*, 2370–2374.
- (7) Case, D. A.; Karplus, M. Dynamics of Ligand Binding to Heme Proteins. *J. Mol. Biol.* **1979**, *132*, 343–368.
- (8) Schnell, J. R.; Dyson, H. J.; Wright, P. E. Structure, Dynamics, and Catalytic Function of Dihydrofolate Reductase. *Annu. Rev. Biophys. Biomol. Struct.* **2004**, *33*, 119–140.
- (9) Oliveberg, M.; Wolynes, P. G. The Experimental Survey of Protein-Folding Energy Landscapes. *Q. Rev. Biophys.* **2005**, *38*, 245–288.
- (10) Roncone, R.; Monzani, E.; Murtas, M.; Battaini, G.; Pennati, A.; Sanangeltoni, A. M.; Zuccotti, S.; Bolognesi, M.; Casella, L. Engineering Peroxidase Activity in Myoglobin: the Haem Cavity Structure and Peroxide Activation in the T67R/S92D Mutant and Its Derivative Reconstituted with Protohaemin-L-Histidine. *Biochem. J.* **2004**, *377*, 717–724.
- (11) Kim, H.; Cho, M. Infrared Probes for Studying the Structure and Dynamics of Biomolecules. *Chem. Rev.* **2013**, DOI: 10.1021/cr3005185.
- (12) Getahun, Z.; Huang, C.-Y.; Wang, T.; De Leon, B.; DeGrado, W. F.; Gai, F. Using Nitrile-Derivatized Amino Acids as Infrared Probes of Local Environment. *J. Am. Chem. Soc.* **2003**, *125*, 405–411.
- (13) Mukherjee, S.; Chowdhury, P.; DeGrado, W. F.; Gai, F. Site-Specific Hydration Status of an Amphipathic Peptide in AOT Reverse Micelles. *Langmuir* **2007**, *23*, 11174–11179.
- (14) Suydam, I. T.; Boxer, S. G. Vibrational Stark Effects Calibrate the Sensitivity of Vibrational Probes for Electric Fields in Proteins. *Biochemistry* **2003**, *42*, 12050–12055.
- (15) Oh, K.-I.; Lee, J.-H.; Joo, C.; Han, H.; Cho, M.  $\beta$ -Azidoalanine as an IR Probe: Application to Amyloid  $\text{A}\beta(16-22)$  Aggregation. *J. Phys. Chem. B* **2008**, *112*, 10352–10357.
- (16) Schultz, K. C.; Supekova, L.; Ryu, Y.; Xie, J.; Perera, R.; Schultz, P. G. A Genetically Encoded Infrared Probe. *J. Am. Chem. Soc.* **2006**, *128*, 13984–13985.
- (17) Fang, C.; Bauman, J. D.; Das, K.; Remorino, A.; Arnold, E.; Hochstrasser, R. M. Two-Dimensional Infrared Spectra Reveal Relaxation of the Nonnucleoside Inhibitor TMC278 Complexed with HIV-1 Reverse Transcriptase. *Proc. Natl. Acad. Sci. U.S.A.* **2008**, *105*, 1472–1477.
- (18) Bagchi, S.; Nebgen, B. T.; Loring, R. F.; Fayer, M. D. Dynamics of a Myoglobin Mutant Enzyme: 2D IR Vibrational Echo Experiments and Simulations. *J. Am. Chem. Soc.* **2010**, *132*, 18367–18376.
- (19) Suydam, I. T.; Snow, C. D.; Pande, V. S.; Boxer, S. G. Electric Fields at the Active Site of an Enzyme: Direct Comparison of Experiment with Theory. *Science* **2006**, *313*, 200–204.
- (20) Lin, Y. S.; Shorb, J. M.; Mukherjee, P.; Zanni, M. T.; Skinner, J. L. Empirical Amide I Vibrational Frequency Map: Application to 2D-IR Line Shapes for Isotope-Edited Membrane Peptide Bundles. *J. Phys. Chem. B* **2008**, *113*, 592–602.
- (21) Kinnaman, C. S.; Creemers, M. E.; Romesberg, F. E.; Corcelli, S. A. Infrared Line Shape of an  $\alpha$ -Carbon Deuterium-Labeled Amino Acid. *J. Am. Chem. Soc.* **2006**, *128*, 13334–13335.
- (22) Lindquist, B. A.; Furse, K. E.; Corcelli, S. A. Nitrile groups as vibrational probes of biomolecular structure and dynamics: an overview. *Phys. Chem. Chem. Phys.* **2009**, *11*, 8119–8132.
- (23) Koziński, M.; Garrett-Roe, S.; Hamm, P. 2D-IR Spectroscopy of the Sulphydryl Band of Cysteines in the Hydrophobic Core of Proteins. *J. Phys. Chem. B* **2008**, *112*, 7645–7650.
- (24) Jansen, T. I. C.; Knoester, J. Waiting Time Dynamics in Two-Dimensional Infrared Spectroscopy. *Acc. Chem. Res.* **2009**, *42*, 1405–1411.
- (25) Waegele, M. M.; Culik, R. M.; Gai, F. Site-Specific Spectroscopic Reporters of the Local Electric Field, Hydration, Structure, and Dynamics of Biomolecules. *J. Phys. Chem. Lett.* **2011**, *2*, 2598–2609.
- (26) Krummel, A. T.; Zanni, M. T. Evidence for Coupling between Nitrile Groups Using DNA Templates: A Promising New Method for Monitoring Structures with Infrared Spectroscopy. *J. Phys. Chem. B* **2008**, *112*, 1336–1338.
- (27) Fafarman, A. T.; Webb, L. J.; Chuang, J. I.; Boxer, S. G. Site-Specific Conversion of Cysteine Thiols into Thiocyanate Creates an IR Probe for Electric Fields in Proteins. *J. Am. Chem. Soc.* **2006**, *128*, 13356–13357.
- (28) Taskent-Sezgin, H.; Chung, J.; Banerjee, P. S.; Nagarajan, S.; Dyer, R. B.; Carrico, I.; Raleigh, D. P. Azidohomoalanine: A Conformationally Sensitive IR Probe of Protein Folding, Protein Structure, and Electrostatics. *Angew. Chem., Int. Ed.* **2010**, *49*, 7473–7475.
- (29) Kiick, K. L.; Saxon, E.; Tirrell, D. A.; Bertozzi, C. R. Incorporation of Azides into Recombinant Proteins for Chemoselective Modification by the Staudinger Ligation. *Proc. Natl. Acad. Sci. U.S.A.* **2002**, *99*, 19–24.
- (30) Ye, S.; Zaitseva, E.; Caltabiano, G.; Schertler, G. F. X.; Sakmar, T. P.; Deupi, X.; Vogel, R. Tracking G-Protein-Coupled Receptor Activation Using Genetically Encoded Infrared Probes. *Nature* **2010**, *464*, 1386–1389.
- (31) Wang, A.; Nairn, N. W.; Johnson, R. S.; Tirrell, D. A.; Grabstein, K. Processing of N-Terminal Unnatural Amino Acids in Recombinant

- Human Interferon- $\beta$  in Escherichia coli. *ChemBioChem* **2008**, *9*, 324–330.
- (32) Choi, J.-H.; Oh, K.-I.; Cho, M. Azido-Derivatized Compounds As IR Probes of Local Electrostatic Environment: Theoretical Studies. *J. Chem. Phys.* **2008**, *129*, 174512.
- (33) Choi, J.-H.; Raleigh, D.; Cho, M. Azido Homoalanine is a Useful Infrared Probe for Monitoring Local Electrostatics and Side-Chain Solvation in Proteins. *J. Phys. Chem. Lett.* **2011**, *2*, 2158–2162.
- (34) Oh, K.-I.; Choi, J.-H.; Lee, J.-H.; Han, J.-B.; Lee, H.; Cho, M. Nitrile and Thiocyanate IR Probes: Molecular Dynamics Simulation Studies. *J. Chem. Phys.* **2008**, *128*, 154504.
- (35) Andrews, S. S.; Boxer, S. G. Vibrational Stark Effects of Nitriles I. Methods and Experimental Results. *J. Phys. Chem. A* **2000**, *104*, 11853–11863.
- (36) Andrews, S. S.; Boxer, S. G. Vibrational Stark Effects of Nitriles II. Physical Origins of Stark Effects from Experiment and Perturbation Models. *J. Phys. Chem. A* **2002**, *106*, 469–477.
- (37) Bublitz, G. U.; Boxer, S. G. STARK SPECTROSCOPY: Applications in Chemistry, Biology, and Materials Science. *Annu. Rev. Phys. Chem.* **1997**, *48*, 213–242.
- (38) Park, E. S.; Andrews, S. S.; Hu, R. B.; Boxer, S. G. Vibrational Stark Spectroscopy in Proteins: A Probe and Calibration for Electrostatic Fields. *J. Phys. Chem. B* **1999**, *103*, 9813–9817.
- (39) Park, E. S.; Andrews, S. S.; Hu, R. B.; Boxer, S. G. Vibrational Stark Spectroscopy in Proteins: A Probe and Calibration for Electrostatic Fields. *Biophys. J.* **2000**, *78*, 284a–284a.
- (40) Silverman, L. N.; Pitzer, M. E.; Ankomah, P. O.; Boxer, S. G.; Fenlon, E. E. Vibrational Stark Effect Probes for Nucleic Acids. *J. Phys. Chem. B* **2007**, *111*, 11611–11613.
- (41) Cho, M. Coherent Two-Dimensional Optical Spectroscopy. *Chem. Rev.* **2008**, *108*, 1331–1418.
- (42) Cho, M. *Two-Dimensional Optical Spectroscopy*; CRC Press: Boca Raton, 2009.
- (43) Devereux, M.; Meuwly, M. Structural Assignment of Spectra by Characterization of Conformational Substates in Bound MbCO. *Biophys. J.* **2009**, *96*, 4363–4375.
- (44) Bagchi, S.; Thorpe, D. G.; Thorpe, I. F.; Voth, G. A.; Fayer, M. D. Conformational Switching between Protein Substates Studied with 2D IR Vibrational Echo Spectroscopy and Molecular Dynamics Simulations. *J. Phys. Chem. B* **2010**, *114*, 17187–17193.
- (45) Schulze, B. G.; Evanseck, J. D. Cooperative Role of Arg45 and His64 in the Spectroscopic A3 State of Carbonmonoxy Myoglobin: Molecular Dynamics Simulations, Multivariate Analysis, and Quantum Mechanical Computations. *J. Am. Chem. Soc.* **1999**, *121*, 6444–6454.
- (46) Merchant, K. A.; Noid, W. G.; Akiyama, R.; Finkelstein, I. J.; Goun, A.; McClain, B. L.; Loring, R. F.; Fayer, M. D. Myoglobin-CO Substate Structures and Dynamics: Multidimensional Vibrational Echoes and Molecular Dynamics Simulations. *J. Am. Chem. Soc.* **2003**, *125*, 13804–13818.
- (47) Hamm, P.; Zanni, M. *Concepts and Methods of 2D Infrared Spectroscopy*; Cambridge University Press: UK, 2011.
- (48) Thielges, M. C.; Fayer, M. D. Protein Dynamics Studied with Ultrafast Two-Dimensional Infrared Vibrational Echo Spectroscopy. *Acc. Chem. Res.* **2012**, *45*, 1866–1874.
- (49) Zheng, J. R.; Kwak, K. W.; Xie, J.; Fayer, M. D. Ultrafast Carbon-Carbon Single-Bond Rotational Isomerization in Room-Temperature Solution. *Science* **2006**, *313*, 1951–1955.
- (50) Chung, H. S.; Khalil, M.; Smith, A. W.; Ganim, Z.; Tokmakoff, A. Conformational Changes during the Nanosecond-to-Millisecond Unfolding of Ubiquitin. *Proc. Natl. Acad. Sci. U.S.A.* **2005**, *102*, 612–617.
- (51) Demirdoven, N.; Cheatum, C. M.; Chung, H. S.; Khalil, M.; Knoester, J.; Tokmakoff, A. Two-Dimensional Infrared Spectroscopy of Antiparallel Beta-Sheet Secondary Structure. *J. Am. Chem. Soc.* **2004**, *126*, 7981–7990.
- (52) Ganim, Z.; Chung, H. S.; Smith, A. W.; DeFlores, L. P.; Jones, K. C.; Tokmakoff, A.; Amide, I. Two-Dimensional Infrared Spectroscopy of Proteins. *Acc. Chem. Res.* **2008**, *41*, 432–441.
- (53) Frauenfelder, H.; McMahon, B. H.; Fenimore, P. W. Myoglobin: The Hydrogen Atom of Biology and a Paradigm of Complexity. *Proc. Natl. Acad. Sci. U.S.A.* **2003**, *100*, 8615–8617.
- (54) Decatur, S. M.; DePillis, G. D.; Boxer, S. G. Modulation of Protein Function by Exogenous Ligands in Protein Cavities: CO Binding to a Myoglobin Cavity Mutant Containing Unnatural Proximal Ligands. *Biochemistry* **1996**, *35*, 3925–3932.
- (55) Rector, K. D.; Engholm, J. R.; Hill, J. R.; Myers, D. J.; Hu, R.; Boxer, S. G.; Dlott, D. D.; Fayer, M. D. Dynamics of Myoglobin–CO with the Proximal Histidine Removed: Vibrational Echo Experiments. *J. Phys. Chem. B* **1998**, *102*, 331–333.
- (56) Alben, J. O.; Fager, L. Y. Infrared Studies of Azide Bound to Myoglobin and Hemoglobin Temperature Dependence of Ionicity. *Biochemistry* **1972**, *11*, 842–847.
- (57) Bogumil, R.; Hunter, C. L.; Maurus, R.; Tang, H.-L.; Lee, H.; Lloyd, E.; Brayer, G. D.; Smith, M.; Mauk, A. G. FTIR Analysis of the Interaction of Azide with Horse Heart Myoglobin Variants. *Biochemistry* **1994**, *33*, 7600–7608.
- (58) Causgrove, T. P.; Dyer, R. B. Protein Response to Photo-dissociation of Carbon Monoxide from Carbon Monoxymyoglobin Probed by Time-Resolved Infrared Spectroscopy of the Amide I Band. *Biochemistry* **1993**, *32*, 11985–11991.
- (59) Danielsson, J.; Meuwly, M. Molecular Dynamics Simulations of CN– Dynamics and Spectroscopy in Myoglobin. *ChemPhysChem* **2007**, *8*, 1077–1084.
- (60) Hirota, S.; Ogura, T.; Shinzawa-Itoh, K.; Yoshikawa, S.; Kitagawa, T. Observation of Multiple CN-Isotope-Sensitive Raman Bands for CN- Adducts of Hemoglobin, Myoglobin, and Cytochrome c Oxidase: Evidence for Vibrational Coupling between the Fe–C–N Bending and Porphyrin In-Plane Modes. *J. Phys. Chem.* **1996**, *100*, 15274–15279.
- (61) Ishikawa, H.; Kwak, K.; Chung, J. K.; Kim, S.; Fayer, M. D. Direct Observation of Fast Protein Conformational Switching. *Proc. Natl. Acad. Sci. U.S.A.* **2008**, *105*, 8619–8624.
- (62) Kriegel, J. M.; Nienhaus, K.; Deng, P.; Fuchs, J.; Nienhaus, G. U. Ligand Dynamics in a Protein Internal Cavity. *Proc. Natl. Acad. Sci. U.S.A.* **2003**, *100*, 7069–7074.
- (63) Lehle, H.; Kriegel, J. M.; Nienhaus, K.; Deng, P.; Fengler, S.; Nienhaus, G. U. Probing Electric Fields in Protein Cavities by Using the Vibrational Stark Effect of Carbon Monoxide. *Biophys. J.* **2005**, *88*, 1978–1990.
- (64) Lim, M.; Jackson, T. A.; Anfinrud, P. A. Mid-infrared Vibrational Spectrum of CO after Photodissociation from Heme: Evidence for a Ligand Docking Site in the Heme Pocket of Hemoglobin and Myoglobin. *J. Chem. Phys.* **1995**, *102*, 4355–4366.
- (65) Olson, J. S.; Phillips, G. N. Kinetic Pathways and Barriers for Ligand Binding to Myoglobin. *J. Biol. Chem.* **1996**, *271*, 17593–17596.
- (66) Vojtechovsky, J.; Chu, K.; Berendzen, J.; Sweet, R. M.; Schlichting, I. Crystal Structures of Myoglobin-Ligand Complexes at Near-atomic Resolution. *Biophys. J.* **1999**, *77*, 2153–2174.
- (67) Johnson, J. B.; Lamb, D. C.; Frauenfelder, H.; Müller, J. D.; McMahon, B.; Nienhaus, G. U.; Young, R. D. Ligand Binding to Heme Proteins. VI. Interconversion of Taxonomic Substates in Carbon-monoxymyoglobin. *Biophys. J.* **1996**, *71*, 1563–1573.
- (68) Li, T.; Quillin, M. L.; Phillips, G. N.; Olson, J. S. Structural Determinants of the Stretching Frequency of CO Bound to Myoglobin. *Biochemistry* **1994**, *33*, 1433–1446.
- (69) Caughey, W. S.; Shimada, H.; Choc, M. G.; Tucker, M. P. Dynamic Protein Structures: Infrared Evidence for Four Discrete Rapidly Interconverting Conformers at the Carbon Monoxide Binding Site of Bovine Heart Myoglobin. *Proc. Natl. Acad. Sci. U.S.A.* **1981**, *78*, 2903–2907.
- (70) Tian, W. D.; Sage, J. T.; Champion, P. M.; Chien, E.; Sligar, S. G. Probing Heme Protein Conformational Equilibration Rates with Kinetic Selection. *Biochemistry* **1996**, *35*, 3487–3502.
- (71) Phillips, G. N.; Teodoro, M. L.; Li, T.; Smith, B.; Olson, J. S. Bound CO Is A Molecular Probe of Electrostatic Potential in the Distal Pocket of Myoglobin. *J. Phys. Chem. B* **1999**, *103*, 8817–8829.

- (72) Fayer, M. D. Fast Protein Dynamics Probed with Infrared Vibrational Echo Experiments. *Annu. Rev. Phys. Chem.* **2001**, *52*, 315–356.
- (73) Nienhaus, G. U.; Mourant, J. R.; Chu, K.; Frauenfelder, H. Ligand Binding to Heme Proteins: The Effect of Light on Ligand Binding in Myoglobin. *Biochemistry* **1994**, *33*, 13413–13430.
- (74) Oldfield, E.; Guo, K.; Augspurger, J. D.; Dykstra, C. E. A Molecular Model for the Major Conformational Substates in Heme Proteins. *J. Am. Chem. Soc.* **1991**, *113*, 7537–7541.
- (75) Ansari, A.; Berendzen, J.; Braunstein, D.; Cowen, B. R.; Frauenfelder, H.; Hong, M. K.; Iben, I. E. T.; Johnson, J. B.; Ormos, P.; Sauke, T. B.; et al. Rebinding and Relaxation in the Myoglobin Pocket. *Biophys. Chem.* **1987**, *26*, 337–355.
- (76) Meuwly, M. On the Influence of the Local Environment on the CO Stretching Frequencies in Native Myoglobin: Assignment of the B-States in MbCO. *ChemPhysChem* **2006**, *7*, 2061–2063.
- (77) Cho, M. Vibrational Solvatochromism and Electrochromism: Coarse-Grained Models and Their Relationships. *J. Chem. Phys.* **2009**, *130*, 094505.
- (78) Choi, J.-H.; Cho, M. Vibrational Solvatochromism and Electrochromism of Infrared Probe Molecules Containing CO, CN, C=O, or C–F Vibrational Chromophore. *J. Chem. Phys.* **2011**, *134*, 154513.
- (79) Lee, H.; Choi, J.-H.; Cho, M. Vibrational Solvatochromism and Electrochromism of Cyanide, Thiocyanate, and Azide Anions in Water. *Phys. Chem. Chem. Phys.* **2010**, *12*, 12658–12669.
- (80) Park, E. S.; Boxer, S. G. Origins of the Sensitivity of Molecular Vibrations to Electric Fields: Carbonyl and Nitrosyl Stretches in Model Compounds and Proteins. *J. Phys. Chem. B* **2002**, *106*, 5800–5806.
- (81) Lee, H.; Choi, J.-H.; Cho, M. Vibrational Solvatochromism and Electrochromism. II. Multipole Analysis. *J. Chem. Phys.* **2012**, *137*, 114307.
- (82) Frisch, M. J.; Trucks, G. W.; Schlegel, H. B.; Scuseria, G. E.; Robb, M. A.; Cheeseman, J. R.; Montgomery, J. A., Jr.; Vreven, T.; Kudin, K. N.; Burant, J. C.; et al. *Gaussian 09*; Gaussian, Inc.: Wallingford, CT, 2004.
- (83) Dalosto, S. D.; Vanderkooi, J. M.; Sharp, K. A. Vibrational Stark Effects on Carbonyl, Nitrile, and Nitrosyl Compounds Including Heme Ligands, CO, CN, and NO, Studied with Density Functional Theory. *J. Phys. Chem. B* **2004**, *108*, 6450–6457.
- (84) Case, D. A.; Darden, T. A.; Cheatham, T. E., III; Simmerling, C. L.; Wang, J.; Duke, R. E.; Luo, R.; Merz, K. M., Jr.; Pearlman, D. A.; Crowley, M.; et al. *AMBER 9*; University of California: San Francisco, 2006.
- (85) Kuriyan, J.; Wilz, S.; Karplus, M.; Petsko, G. A. X-ray Structure and Refinement of Carbon-Monoxy (Fe II)-Myoglobin at 1.5 Å Resolution. *J. Mol. Biol.* **1986**, *192*, 133–154.
- (86) Anselmi, M.; Brunori, M.; Vallone, B.; Di Nola, A. Molecular Dynamics Simulation of Deoxy and Carboxy Murine Neuroglobin in Water. *Biophys. J.* **2007**, *93*, 434–441.
- (87) Darden, T.; York, D.; Pedersen, L. Particle Mesh Ewald—an N.Log(N) Method for Ewald Sums in Large Systems. *J. Chem. Phys.* **1993**, *98*, 10089–10092.
- (88) Kubo, R. A Stochastic Theory of Line-Shape and Relaxation. *Adv. Chem. Phys.* **1969**, *15*, 101.
- (89) Mukamel, S. *Principles of Nonlinear Optical Spectroscopy*; Oxford University Press: Oxford, 1995.
- (90) Hill, J. R.; Ziegler, C. J.; Suslick, K. S.; Dlott, D. D.; Rella, C. W.; Fayer, M. D. Tuning the Vibrational Relaxation of CO Bound to Heme and Metalloporphyrin Complexes. *J. Phys. Chem.* **1996**, *100*, 18023–18032.
- (91) Dlott, D. D.; Fayer, M. D.; Hill, J. R.; Rella, C. W.; Suslick, K. S.; Ziegler, C. J. Vibrational Relaxation in Metalloporphyrin CO Complexes. *J. Am. Chem. Soc.* **1996**, *118*, 7853–7854.
- (92) Hill, J. R.; Dlott, D. D.; Fayer, M. D.; Peterson, K. A.; Rella, C. W.; Rosenblatt, M. M.; Suslick, K. S.; Ziegler, C. J. Vibrational Relaxation of Carbon-Monoxide in Model Heme Compounds—6-Coordinate Metalloporphyrins (M = FE, RU, OS). *Chem. Phys. Lett.* **1995**, *244*, 218–223.
- (93) Thielges, M. C.; Chung, J. K.; Axup, J. Y.; Fayer, M. D. Influence of Histidine Tag Attachment on Picosecond Protein Dynamics. *Biochemistry* **2011**, *50*, 5799–5805.
- (94) Kwac, K.; Cho, M. Two-Color Pump-Probe Spectroscopies of Two- and Three-Level Systems: 2-Dimensional Line Shapes and Solvation Dynamics. *J. Phys. Chem. A* **2003**, *107*, 5903–5912.
- (95) Kwak, K.; Rosenfeld, D. E.; Fayer, M. D. Taking Apart the Two-Dimensional Infrared Vibrational Echo Spectra: More Information and Elimination of Distortions. *J. Chem. Phys.* **2008**, *128*, No. 204505.
- (96) Fenn, E. E.; Fayer, M. D. Extracting 2D IR frequency-frequency correlation functions from two component systems. *J. Chem. Phys.* **2011**, *135*, No. 074502.
- (97) Kwak, K.; Zheng, J. R.; Cang, H.; Fayer, M. D. Ultrafast two-dimensional infrared vibrational echo chemical exchange experiments and theory. *J. Phys. Chem. B* **2006**, *110*, 19998–20013.
- (98) Finkelstein, I. J.; Goj, A.; McClain, B. L.; Massari, A. M.; Merchant, K. A.; Loring, R. F.; Fayer, M. D. Ultrafast Dynamics of Myoglobin without the Distal Histidine: Stimulated Vibrational Echo Experiments and Molecular Dynamics Simulations. *J. Phys. Chem. B* **2005**, *109*, 16959–16966.